

ABSTRACT

Title of Document: EXPLOITING PROCESS SYNERGY
BETWEEN ANODIC ALUMINUM OXIDE
NANOTEMPLATES AND ATOMIC LAYER
DEPOSITION: FROM THIN FILMS TO 3D
NANO-ELECTRONIC DEVICES

Parag Banerjee, Doctor of Philosophy, 2011

Directed By: Professor Gary W. Rubloff
Minta Martin Professor of Engineering,
Department of Materials Science and
Engineering & the Institute for Systems
Research

ABSTRACT: Self-assembled, 3D nanoporous templates present an opportunity to develop devices which are lithography-free, massively scalable and hence, highly manufacturable. Self-limited deposition processes on the other hand, allow functional

thin films to be deposited inside such templates with precision and unprecedented conformality. Taken together, the combination of both processes provides a powerful ‘toolbox’ to enable many modern nano devices.

In this work, I will present data in three parts. First, I will demonstrate the capabilities of Atomic Layer Deposition (ALD), a self-limited thin film deposition technique in preparing nanoalloyed Al-doped ZnO (AZO) thin films. These films are visibly transparent *and* electrically conducting. Structure-property relationships are established that highlight the power of ALD to tailor film compositions at the nanoscale.

Next, I will use ALD ZnO films in conjunction with aged, ALD V₂O₅ films to form pn junctions which show rectification with an $I_{\text{on}}/I_{\text{off}}$ as high as 598. While, the ZnO is a well known n-type semiconductor, the discovery of p-type conductivity in aged V₂O₅ is surprising and is found to be due to the protonic (H⁺) conductivity of intercalated H₂O in V₂O₅. Thus, we demonstrate a mixed electronic-ionic pn junction for the first time.

Finally, I combine the material set of the pn junction with self-assembled, anodic aluminum oxide (AAO) 3D nanoporous templates to create 3D nanotubular pn junctions. The pn junctions are built inside pores which are only 90nm wide and up to 2μm deep and show rectification with $I_{\text{on}}/I_{\text{off}}$ of 16.7.

Process development and integrations strategies will be discussed that allow for large scale manufacturing of such devices a real possibility.

EXPLOITING PROCESS SYNERGY BETWEEN ANODIC ALUMINUM OXIDE
NANOTEMPLATES AND ATOMIC LAYER DEPOSITION: FROM THIN FILMS
TO 3D NANO-ELECTRONIC DEVICES

By

Parag Banerjee.

Dissertation submitted to the Faculty of the Graduate School of the
University of Maryland, College Park, in partial fulfillment
of the requirements for the degree of
Doctor of Philosophy,
2011

Advisory Committee:

Professor Gary W. Rubloff, Chair

Professor Eric Wachsman

Professor Lourdes Salamanca-Riba

Professor Ichiro Takeuchi

Professor Sang Bok Lee

© Copyright by

Parag Banerjee

2011

Dedication

Because of Bapi and Ma, for Jaana, Idi and Avi ...

Acknowledgements

The work presented in this thesis and beyond, represents a string of fortuitous events that started in the February of 2006 with a phone conversation with Gary - one that I had to take in a parking lot at Micron Technology Inc., Boise. The conversation lasted for 1.5 hours. Five years since and a dozen publications, a few patents and the opening of an Energy Frontier Research Center (EFRC) later, I stand ready to launch a career that I had always wished for. No one has a bigger hand in this than my mentor and my advisor Professor Gary W. Rubloff. For his unflinching support, guidance and belief in me, I will forever be grateful!

During my stay on campus I have come across brilliant minds. Their work, knowledge and eagerness to support me has been inspirational. Professor Sang Bok Lee has taught me whatever little I know about electrochemistry and more importantly, how to dream and think big. My professors in Materials Science & Engineering will be my role models for teachers and I can only hope I can capture their dedication, passion and eloquence in class. A special word of thanks is also due for Professor Dawn A. Bonnell at the University of Pennsylvania for taking me under her wings for two months in the spring of 2009 and showing me the power of doing simple but effective experiments.

My last, but certainly not least words of gratitude are reserved for the one person in life who has helped me truly enjoy my 5 years in graduate school. To my dearest wife, Geetanjali who helped put bread on the table while I burnt the midnight oil, I promise I will never go back to graduate school again!

Table of Contents

Dedication	ii
Acknowledgements	iii
Table of Contents	iv
Chapter 1: Introduction	1
Past Work:.....	3
Objective:	5
Organization of the thesis:	6
Chapter 2: Anodic Aluminum Oxide (AAO).....	8
Introduction:.....	8
Structure of AAO:.....	8
Processing of AAO:	12
Two-step anodization method:.....	12
Pore widening:	13
Physico-chemical processes in AAO:.....	14
Electrical signature of anodization:.....	14
Chemical reactions during a nodization:.....	16
Self-assembly of nanopores:.....	17
Chapter 3: Atomic Layer Deposition (ALD)	19
Introduction:.....	19
Applied ALD research, I – Multicomponent films:.....	22
Applied ALD research II – 3D Nanostructures	28

Chapter 4: Structural, Electrical and Optical properties of ALD Al-doped ZnO Films	32
.....	32
Abstract:	32
Introduction:.....	32
Experimental:	34
Results and Discussion:	37
Phenomenological model for at% Al doping:.....	37
X-ray Diffraction Data:.....	38
AFM and Surface Roughness:	42
Hall Measurements:	43
Optical Properties.....	45
Analysis and Discussion:	47
Conclusion	49
Chapter 5: Atomic layer deposition of p-V ₂ O ₅ .nH ₂ O for rectifying p-V ₂ O ₅ /n-ZnO diodes	51
.....	51
Abstract:	51
Introduction:.....	51
Experimental Details:.....	53
Device Fabrication:	53
Samples and Equipment for Characterization:.....	54
Results:.....	55
V ₂ O ₅ Film Structure:.....	55
Electrical characterization of V ₂ O ₅ and ZnO films.....	58

Electrical characterization of V ₂ O ₅ – ZnO junctions	60
Discussion:	63
Conclusions:.....	68
Chapter 6: Three-dimensional nanotubular diodes using integrated atomic layer deposition scheme	70
Abstract:	70
Introduction:.....	70
Experimental Details:.....	71
Results and Discussion:	74
Conclusions:.....	77
Chapter 7: Conclusions and scope for future work.....	78
Appendix 1	81
Example of Process Recipe in BENEQ TFS 500	81
Appendix 2	87
Appendix 3	88
Bibliography.....	89

Chapter 1: Introduction

Nanotechnology marks human civilization's pinnacle in technological achievement, driven largely in part by our understanding of matter and its interaction with the environment. This knowledge has finally given us the ability to manipulate structure at the atomic level and has led to the synthesis of new materials with a fascinating array of properties. Integrating such materials into the many facets of our society has led us to dramatically improve the quality of our lives.

While science continues to provide the impetus for new discoveries, the engineering challenge is to integrate such discoveries into modern technology. In this regard, technologies that will be successful eventually are those which reduce process complexity thus reducing equipment costs, while providing process flexibility thereby increasing usability and reducing materials cost. Efficient economics, not surprisingly therefore, is the driver for viable nanotechnology.

An attractive way to achieve the objective of advancing technology at reduced cost is to conceive of processes that are, by their very nature, '*intelligent*' in their design and performance. Intelligent processing schemes are processes which take advantage of inherent driving forces in a physical transformation or a chemical reaction to achieve specific goals. These goals could be as diverse as the buckling of films to produce nanostructures on the surface of a substrate,^[1] or the assembly of copolymers into fine nano-patterns as a result of the minimization of free energy.^[2] Whatever the end objective, intelligent processing schemes provide a facile and elegant way to achieve these processing goals.

In this doctoral work, two such processing schemes are presented and their interplay on one another is exploited to produce novel electronic devices. The first process is termed anodic aluminum oxide (AAO) – a process for making nanoporous templates and will be explained in detail in chapter 2. These templates *self-assemble* during electrochemical oxidation (anodization) on the surface of pure aluminum. The self-assembly results in the formation of hexagonally ordered nanopores (35nm-200nm wide) and is a facile technique requiring none of the expensive lithography steps usually associated with modern semiconductor devices.

The second process is called atomic layer deposition (ALD) and will be explained in detail in chapter 3, where the process will be introduced formally. For now, suffice it is know that ALD is a gas phase deposition process that has the unique ability to *self-limit* the deposition once all surface reaction sites are saturated with the exposed, reactant species. The process also provides monolayer (ML) control of film thickness and is thus an attractive deposition technique for depositing precise, ultra-thin films. Finally, the process requires moderate vacuum conditions – which helps in reducing equipment and hence, capital costs.

Taken together, the combination of self-assembled templates and self-limiting deposition technology provides a powerful, synergistic combination of processes that can produce modern nanoelectronic devices with vastly improved performance metrics and at a fraction of the cost of current devices. This is explained below, via our past work and expertise in this field.

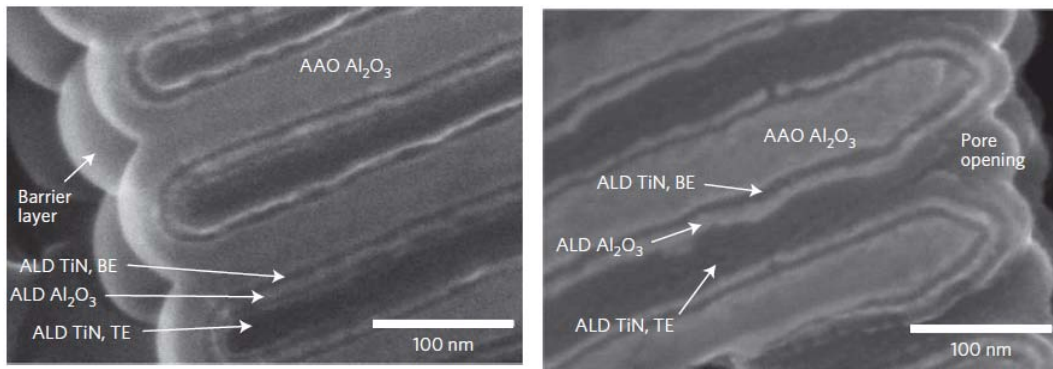


Figure 1. 1. SEM cross-sections of MIM capacitors. Left, bottom of AAO showing the three layers corresponding to the metal (TiN), insulator (Al_2O_3) and the metal (TiN). Right, pore openings at the top also show a similar trilayer structure. (taken from Nat. Nanotech., Banerjee et al.^[3])

Past Work:

It has been shown that utilizing self-assembled nanotemplates as scaffolds for preparing 3D devices can lead to large improvements in the performance of traditional devices.^[3, 4] Thus for example, when AAO nanoporous templates are used to build nanotubular metal-insulator-metal (MIM) capacitors, record high capacitances of $100\mu\text{F}/\text{cm}^2$ and hence high energy densities (recalling that energy, $E = \frac{1}{2} CV^2$, where C = capacitance and V = applied voltage across a capacitor) of 0.7 W.hr/kg can be achieved. Such high capacitance and energy storage is a direct result of increased surface area achieved as a result of the use of the AAO templates, where enhancements of up to 100X are achieved per unit planar surface area. The cross section SEM of such a device is shown in **Figure 1. 1.**

The MIM films ‘packed’ inside AAO templates are deposited using ALD, where the self-limited processing characteristic of ALD is exploited to deposit thin, defect free films deep inside the narrow and high aspect ratio (aspect ratio = ratio of length of pore to diameter of pore) pores of the AAO template. The processing sequence for preparing such nanotubular MIM capacitors is shown in **Figure 1. 2**. Thus, the use of self-assembled AAO templates in conjunction with self-limited ALD processing allows one to vastly improve upon the capacitance of MIM devices and is the foundation on which we base our current work.

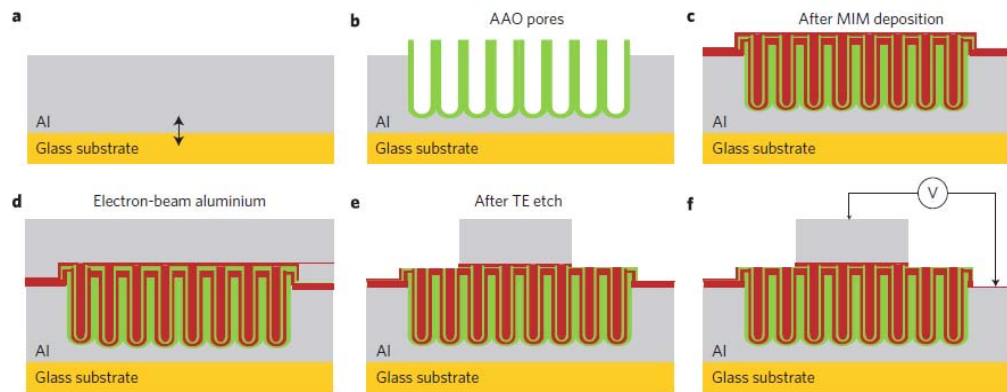


Figure 1. 2: Process sequence to prepare MIM capacitors. a, Al foil is anodically bonded to a glass substrate. b, AAO pore formation. c, MIM deposition via ALD processes. d, Electron-beam Al is deposited on top. e, Photolithography, masking and etching of the Al electrode, then the top electrode (TE) TiN, to define the capacitor area. f, Electrical testing using the Al foil (which is in contact with the bottom electrode TiN) as a back contact and electron-beam Al as the top contact. (taken from Nat. Nanotech., Banerjee et al.^[3])

Objective:

The aim of this work is to expound the process integration of AAO and ALD in the context of another two terminal device – a ‘diode’. A diode, also known as a rectifier, is an electronic equivalent of a valve that conducts electricity (i.e., flow of electrons) when biased under a certain polarity (forward bias). Such a device is most easily built by contacting two semiconductor materials – an n-type semiconductor which conducts electricity via electrons and a p-type semiconductor which conducts via holes. Pn junctions also find application far beyond the act of rectifying electron flow and form the basis for a variety of electronic components such as light-emitting diodes (LEDs)^[5] and photovoltaics (PVs).^[6] While the materials used for making pn junctions can range from high-quality, single crystalline semiconductor materials such as Si and GaAs to oxide semiconductors^[7], polymers^[8] and single molecules,^[9] the physics of pn junctions has been fully explained in standard text-books.^[10]

It is to be noted further that diodes and capacitors together form the basic building block of modern complex digital circuits. Thus, our past demonstration of workable MIM capacitors (as demonstrated in the previous section) and our current attempt to make semiconductor oxide-based diodes lays the foundation for using:

- a) Novel 3D nanoarchitectural designs using self-assembled and self-limiting processing techniques and
- b) Incorporating newer materials in the design and fabrication of modern electronic devices.

Organization of the thesis:

The thesis is organized as follows. First, the foundations for the two technologies that are the underpinnings of this work, namely AAO and ALD are detailed. Next, the experimental work pertaining to this thesis is presented. The first half of this work is devoted to the process development and structure-property relationships in ALD thin films (namely Al-doped ZnO). The next half is devoted to incorporating ALD films into an electronic device. The collected experimental work are essentially formatted reprints of either published or original journal articles that are currently under review. As a result, the language and formatting of the journal articles is retained without significant editing.

The process and theoretical framework for AAO is laid out in Chapter 2, while the details on process and technology for ALD is laid out in Chapter 3. It is to be borne in mind that both AAO and ALD have a prolific list of excellent review articles already available in literature and thus it is not the author's intention to exhaustively re-review this topic. Only the subject matter pertinent to this work is touched upon while providing a listing of further references, where necessary.

Chapter 4 discusses the use of ALD to prepare transparent conducting oxides (TCO's) comprising of Al-doped ZnO (AZO). This paper tracks the structure and properties of AZO films from 0at% to 24at% of Al in ZnO. Strong correlations are observed between structural, electrical and optical properties of these films and are explained within the current theoretical framework of semiconductor physics. The results were published in 2010 in the Journal of Applied Physics.^[11]

Chapter 5 discusses an integrated ALD approach to prepare pn junction diodes comprising of ZnO-V₂O₅. The novel and interesting aspect of this paper is the discovery of a new mechanism for the workings of a pn junctions. While the n-type ZnO is electronically conducting, V₂O₅ can be made to be a p-type conductor by intercalating it with H₂O. It is thought that the H⁺ (protonic species) is then responsible for the p-type behavior. Thus, the diode behaves as a mixed electronic-ionic device and is the first demonstrated rectifier in these class of devices. This paper has been submitted to Advanced Functional Materials as a full-length article and is currently under review.

Chapter 6 details the preparation and properties of 3D nanotubular pn junctions by successfully preparing AZO-V₂O₅ diodes inside AAO templates. This paper is currently under preparation and will be submitted to Applied Physics Letters, shortly.

Finally, chapter 7 provides a concise summary of the work described in this thesis and proposes new ideas for future work.

Chapter 2: Anodic Aluminum Oxide (AAO)

Introduction:

Anodic aluminum oxide (AAO) membrane is a popular, self-assembled platform for templating a variety of nanostructures with applications in energy,^[12] catalysis,^[13] biosensing,^[14] etc. By anodizing high purity Al foils in weakly acidic solutions, one can create a high density of hexagonally arranged nanopores with a variety of pore diameters (D_{pore}), interpore distances (D_{int}) and pore depths of up to hundreds of microns. The porous structure can be removed from the underlying substrate to produce membranes or allowed to remain on the Al foil as a hard, corrosion-resistant layer. Depositing (top-down) or growing (bottom-up) materials within the pores can result in the creation of nanostructures which have found uses in batteries,^[15, 16] capacitors,^[3, 17] photovoltaic devices^[12, 18] and catalyst membranes,^[19] to name a few. Thus, the biggest advantage of using AAO is the access to self-assembled, lithography free, high-density, periodic, precise and easily scalable nanostructures.

In this chapter we will review the basic structure of the AAO, its processing scheme and most importantly, the physico-chemical reactions that lend AAO its characteristic high density, hexagonally self-ordered, nanoporous structure.

Structure of AAO:

AAO consists of a high density of hexagonally ordered nanopores, separated by the Al_2O_3 pore wall, grown on the surface of Al. The schematic of the structure is shown in **Figure 2. 1**. The top-down SEM image is shown in **Figure 2. 2, left**, while a cross section of the same is shown in **Figure 2. 2, right**.

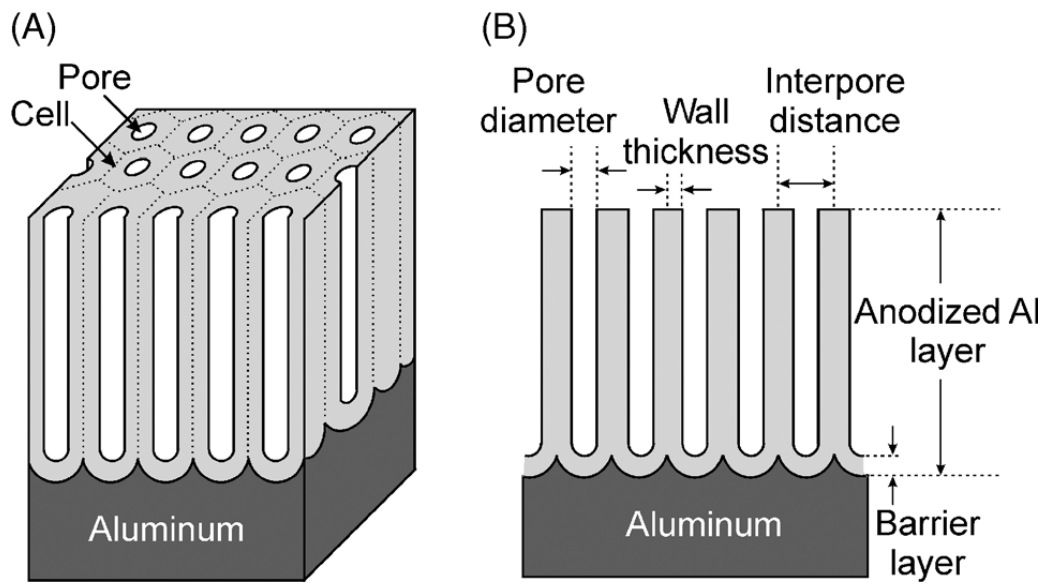


Figure 2. 1: Schematic of an AAO structure where A) shows the 3D structure of the pores, the cell structure and the underlying Al and B) shows the cross section and the various parameters that define the template. A adapted from Eftekhari.^[20]

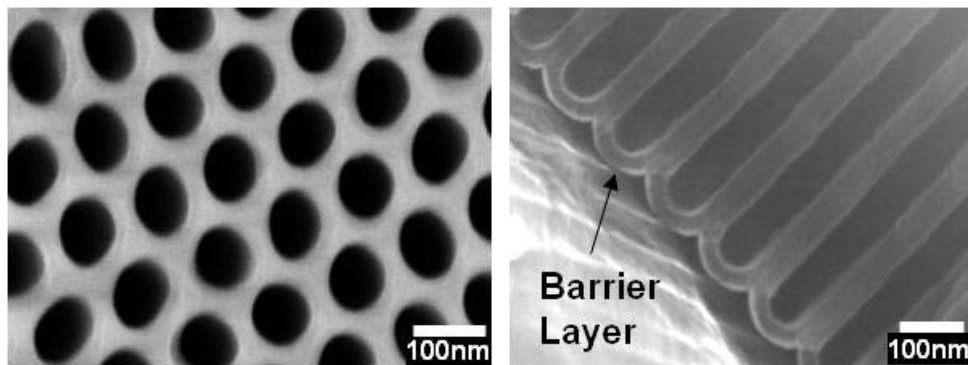


Figure 2. 2: High resolution SEM images of top down (left) and the cross-section (right) of AAO pores grown in oxalic acid. The pores were pore widened after growth. The interpore distance is 110nm and the pore density is 10^{10} cm^{-2} .

Every pore is embedded in a hexagonal cell structure. The cell walls are made of Al_2O_3 which run parallel along the entire length of the template and terminate at the bottom of the pores in hemispherical shells termed as the barrier layer (BL). The BL has tremendous significance in the mechanism of formation, structure and size of the AAO formed and will be discussed later.

The physical parameters of importance in an AAO are D_{pore} , D_{int} and BL thickness (D_{BL}). These parameters are related empirically to the anodization voltage via simple, linear relationships as -

$$D_{\text{pore}} = \lambda_{\text{pore}} \cdot V \quad \mathbf{1}$$

$$D_{\text{int}} = \zeta_p \cdot V \quad \mathbf{2}$$

and

$$D_{\text{BL}} = \alpha_1 + \alpha_2 \cdot V \quad \mathbf{3}$$

where, $\lambda_{\text{pore}}=1.29 \text{ nm V}^{-1}$, $\zeta_p=2.5 \text{ nm V}^{-1}$, $\alpha_1 = 5.9\text{nm}$ and $\alpha_2 = 0.9\text{nm V}^{-1}$ (values of α_1 and α_2 are valid for oxalic acid templates at 20°C and for $V < 57\text{V}$) and are proportionality constants.^[21] Knowing these three parameters allows one to calculate other parameters such as pore wall thickness, cell width and porosity via simple geometrical relationships.^[20] A graphical representation of the variation of D_{pore} and D_{BL} is shown in **Figure 2.3** and provides a comprehensive list of electrolyte solutions and corresponding pore dimensions achievable via AAO.

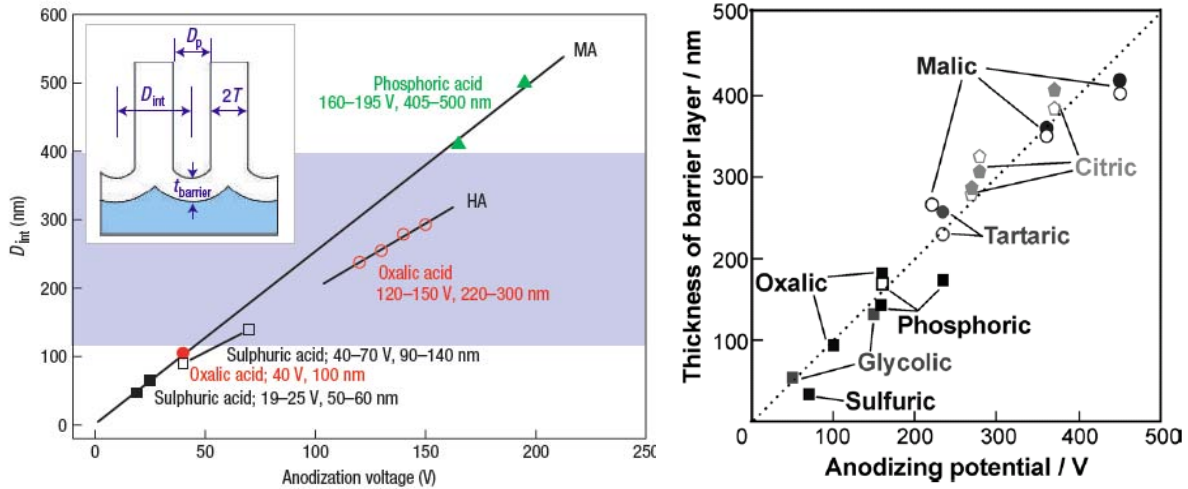


Figure 2. 3: Left, variation of D_{int} with anodization voltage (adapted from Lee et al.^[22]). Right, variation of D_{BL} with anodization voltage (adapted from Chu et al.^[23])

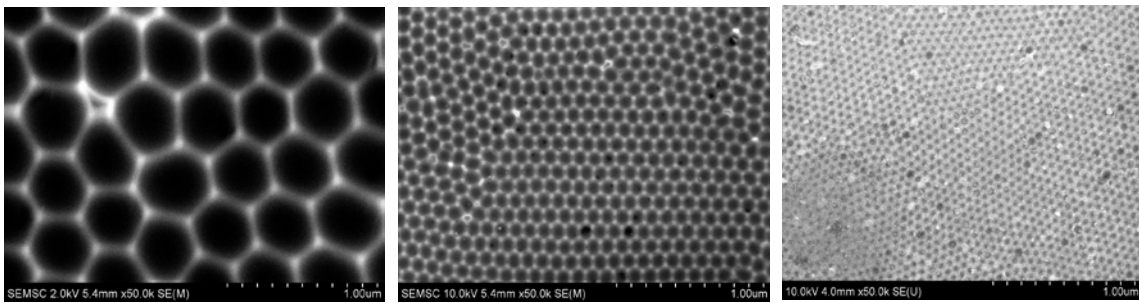


Figure 2. 4: Example of three AAO templates grown with three different electrolyte solutions in the present work. Left - phosphoric acid, middle – oxalic acid and right – sulphuric acid. The magnification used on all three SEM was 50kX. The variation in pore size and density can easily be seen.

Processing of AAO:

Two-step anodization method:

AAO processing usually involves three basic steps. The procedure adopted is one famously proposed by Masuda and is known as the two-step anodization method.^[24]

1. First, high purity Al foils (> 99.99%) are electropolished using 1:5 by volume of HClO₄:C₂H₅OH (perchloric acid : ethanol) solution. This process is carried at 4°C at 15V for at least 5 minutes. The electropolishing removes any surface contaminants as well as the native Al₂O₃ layer formed on Al. The result is a surface which is atomically clean.^[25]
2. Next, the Al foils are subjected to a first anodization step. For the purpose of all the data reported in this thesis, only oxalic acid ((COOH)₂) templates are used. These templates have D_{pore} = 50nm and D_{int} = 110nm. The process is done in 0.3M (COOH)₂ at 8°C and at 40V anodization potential. The duration of the 1st anodization step is 7 hours long which grows approximately 30µm thick film. This film is then subsequently etched in an etchant consisting of 7:18:75 by volume of phosphoric acid: chromic acid: DI water. The etchant temperature is set to 60°C and the etching time is at least 5 hours long.
3. At this point, the surface of the etched Al surface is highly ‘scalloped’ but ordered into hexagonal divots. The base of the scalloped surfaces will initiate new pore formation and thus, the Al substrate is ready for a 2nd anodization step which is the templating process that results in the highly ordered nanoporous structures inside which devices will be formed. This step is

carried out in 0.3M (COOH)₂ solution and under the same conditions in which the 1st anodization is performed.

Pore widening:

The term ‘pore widening’ (PW) refers to the wet isotropic etching of the AAO template performed post anodization. The effect of PW is to open up the pores and maximize the fill space in the nanotemplates for deposition and growth of materials. It also helps to remove the impure Al₂O₃ cell wall which forms on the inner side of the pore walls.

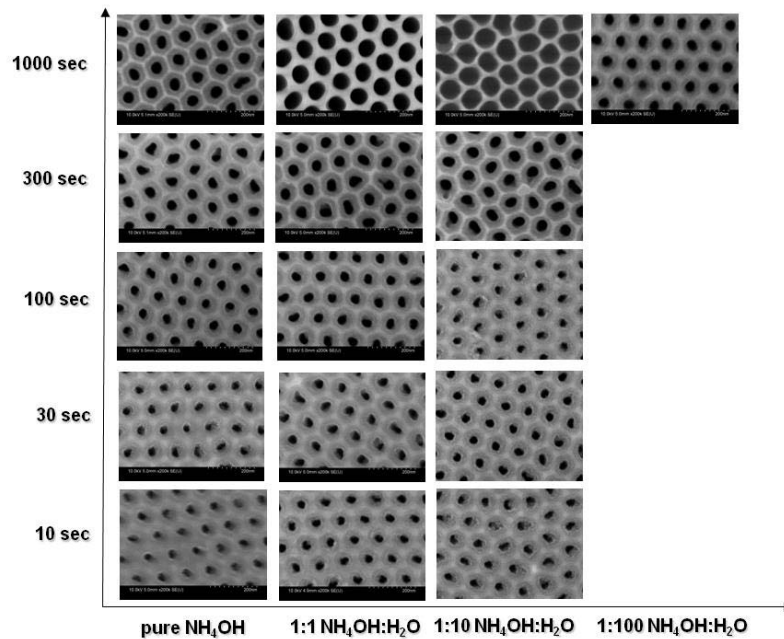


Figure 2. 5: Etch matrix of oxalic acid-based AAO templates subjected to various etch solutions (X-axis) for various times (Y-axis). The best morphology (widest pores and removal of impure part of the cell-wall) is obtained for 1:1 NH₄OH:H₂O at 1000 seconds.

The most common etchant used for PW is phosphoric acid (H_3PO_4).^[26-28] In our experiments we have refrained from using acid-based PW etchants due to PO_4^{3-} ion contamination of our electronic devices. Since Al_2O_3 is amphoteric in nature we use base etchants, specifically NH_4OH with DI water. The experimental results are shown in a matrix form in **Figure 2. 5**. We find that the PW step for 1:1 $NH_4OH:H_2O$ for 1000 seconds gives the best pore morphology. Further, cross section SEM prove (not shown) that there are no residual crystallite formation within the pores as is commonly found for base etchants such as NaOH.

Physico-chemical processes in AAO:

As stated earlier, the biggest advantage of using AAO as a nanotemplate is its ability to self-assemble. To understand why self-assembly in AAO occurs, it is important to understand the physical and chemical reactions occurring during anodization. In this section, we will initially review the electrical signature of AAO during anodization and relate it to the physical changes occurring on the template. Then we will look at the chemical reactions involved in pore formation and finally review two popular models which help explain why natural self-assembly occurs in AAO templates.

Electrical signature of anodization:

We will discuss the case of a potentiostatic (constant voltage) anodization for AAO templates, although galvanostatic (constant current) modes are also prevalent in literature. The choice of choosing one mode of anodization over the other is simply a matter of past precedence set in a lab.

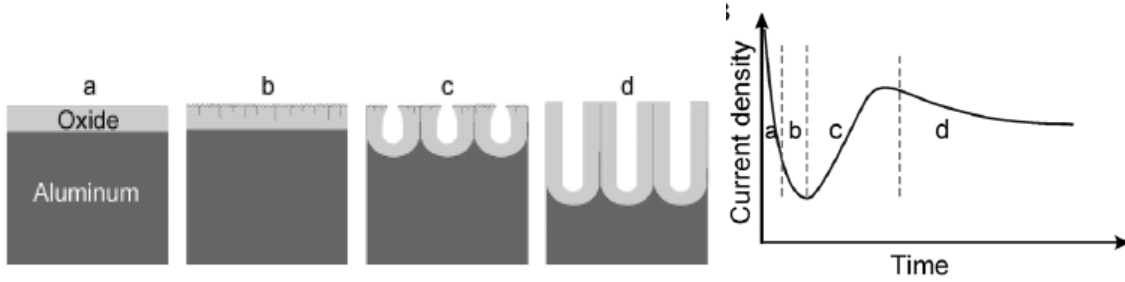
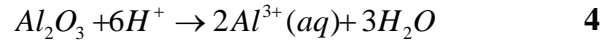


Figure 2. 6: Left, schematic of the various stages of AAO growth starting from the formation of a thick oxide layer (a) at the beginning of the anodization process to crack formation (b) and eventual pore formation and growth(c and d). Right, the current-time signature of the various stages of AAO growth. (reprinted from Eftikhari^[20]).

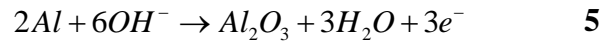
During the initial stages of anodization, a thick oxide layer is formed on the surface of the Al. This causes a sharp decrease in the current (**Figure 2. 6, right**). However, due to the presence of a slightly acidic electrolyte, high anodization voltage and film stress, penetration paths and cracks are created randomly in the film. The crack tips form regions of higher electric field concentration and result in local field assisted dissolution of the oxide layer film at the crack tips. This causes the reduction in film thickness and an increase in current at the crack tips which in turn causes oxide growth and dissolution mechanisms to self-sustain each other. Finally, the current equilibrates to a steady-state value corresponding to equal rates of dissolution and growth at the widened crack tips. The widened crack tips are the initiation points for larger pores.

Chemical reactions during anodization:

Under steady state growth conditions, all reactions occur at the pore tip and across the BL. This is the region where maximum electric field is present and ions drift across the BL reacting at the two interfaces, namely the Al/oxide (AO) interface and the oxide/electrolyte (OE) interface. Two sets of ion migration occur. Al^{3+} ions drift towards the OE interface and finally get ejected into the electrolyte. This results in the dissolution of the Al_2O_3 film and is given as^[29] –



The O^{2-}/OH^- ion, on the other hand, drifts towards the AO interface. The nature of the anionic species (whether O^{2-} or OH^-) is still an open question in literature.^[20] However, it is generally understood that one or the other species reacts with the available Al atom to form Al_2O_3 given as (for the OH^- case) –



These ideas are shown in **Figure 2. 7** below.

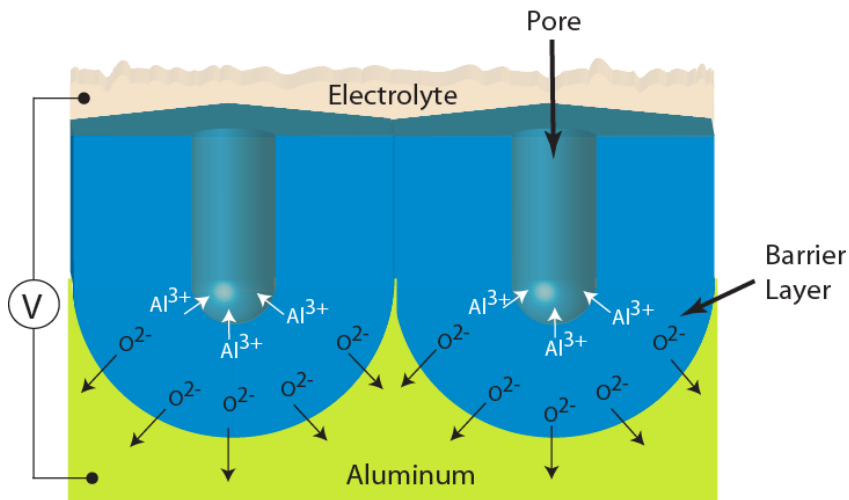


Figure 2. 7: Schematic showing the Al^{3+} and O^{2-} ion migration within the BL

It is to be stressed that during pore growth and under steady state, these reactions occur simultaneously. That is, the rate of oxide growth at the AO interface matches the rate of oxide dissolution at the OE interface. It is the dynamic equilibrium of both these processes that impart AAO templates its unique ability to self assemble. In light of the above discussion, we will now review the mechanism of self-assembly.

Self-assembly of nanopores:

Although many possible theories^[30] have been proposed to explain the nature of self-assembly in AAO, we will, for the sake of brevity, review two popular theories on AAO self-assembly.

The first theory proposed by Chen et al.,^[31] creates a simple electrostatic model of the field-assisted dissolution and growth rates of the BL. In this approach the authors calculate the electric field (E) at the AO and OE interface using simple electrostatics. It is found that –

$$E_{AO} = \frac{r_{pore}}{r_{pore} + D_{BL}} \cdot \frac{V}{D_{BL}} \quad \mathbf{6}$$

$$E_{OE} = \frac{r_{pore} + D_{BL}}{r_{pore}} \cdot \frac{V}{D_{BL}} \quad \mathbf{7}$$

Thus, whenever the radius of the pore, r_{pore} decreases from its equilibrium value, the electric field at the oxide electrolyte interface, E_{OE} increases thereby causing the field assisted dissolution rates to increase. The increased dissolution rates cause r_{pore} to increase again. Similar arguments can be made for changes in D_{BL} as well. The

essential idea of the self-adjusting behavior in this model being - changes to the pore tip morphology leads to electric field changes which counteract the physical changes.

The second theory proposed by Jessensky et al.^[32] and Nielsch et al.^[33] use mechanical stress and the volume expansion associated with the AAO template formation as reasons for self-assembly and ordering. They argue that because the anodization process involves growth of Al_2O_3 on Al, there is volume expansion associated with the process. Further, since on a planar substrate all pores grow at the same time, the Al_2O_3 has nowhere to expand but to rise vertically. This creates mechanical stress in between the cell walls. The equilibration of the stress then leads to the self-ordering behavior of the AAO. Nielsch et al.^[33] have further shown that the greatest ordering of the pores occur when moderate increases in volume change occur (~1.2 of the original volume). This volume change corresponds to a porosity of 10%. The porosity rule is found to be true across different electrolytes as well.

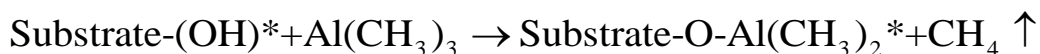
Chapter 3: Atomic Layer Deposition (ALD)

Introduction:

This chapter is a review of ALD technology to the extent that is relevant for the subsequent chapters of the thesis and in the context of the work done by the author. The reader is referred to many excellent, exhaustive and recent reviews on ALD for further, in-depth reading.^[34-39] We start with a brief description of the ALD process and its two main characteristics, namely thickness control and self-limiting behavior. Using these two characteristics, many applications of ALD in modern nanotechnology research is highlighted while simultaneously laying the groundwork to understand much of the experimental work in subsequent chapters.

Atomic Layer Deposition (ALD) has become a popular thin film deposition technology in applications which require precise ultrathin, pin-hole free films. Further, in applications which demand conformal coverage of films inside complex geometries and porous 3D nanostructures, ALD's non line-of-sight deposition is proving to be very valuable. These two properties of ALD films are rapidly opening doors for new and exciting applications.

ALD allows monolayer (ML)-by-ML growth of materials using a cyclical sequence of chemisorption of two or more precursor molecules from the gas phase onto the surface of a substrate. The ALD processing sequence is shown in



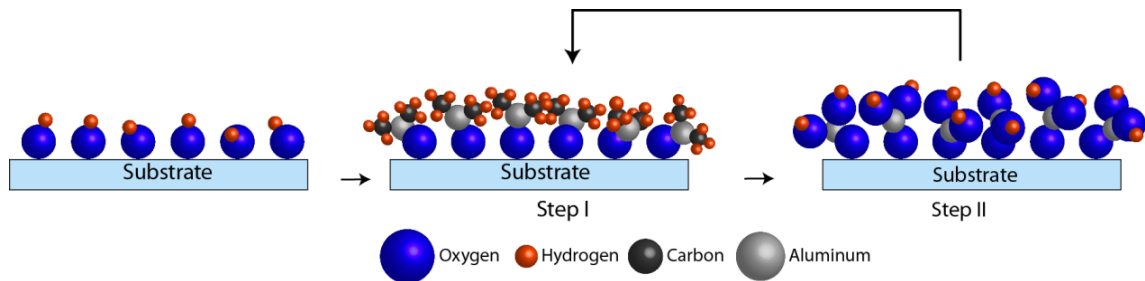
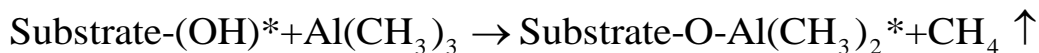
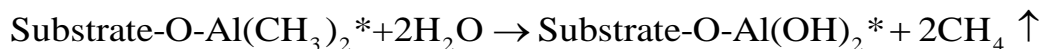


Figure 3. 1. Sequence of surface terminations during ALD deposition of Al₂O₃. Step I shows TMA reacting with surface -OH forming a -CH₃ terminated surface. In Step II, the -CH₃ surface reacts with H₂O leaving a regenerated -OH terminated surface.

for Al₂O₃ growth on a hydroxylated (-OH terminated) surface. In the first step, the -OH terminated surface is exposed to trimethyl aluminum, Al(CH₃)₃ -



In the second step, H₂O is exposed to the -CH₃ terminated surface as –



This reaction thus results in the formation of one ML of Al₂O₃ (~ 1.1Å) and the retrieval of the original -OH surface termination. Both the dosing steps (TMA and H₂O) are separated by a purge step in which an inert gas (N₂ or Ar) is purged into the system to remove any residual, unreacted gas. This step ensures that reaction during subsequent gas dosing steps occur only at the surface of the substrate and not spuriously in gas phase (as in the case of Chemical Vapor Deposition (CVD)).

We now discuss two striking characteristics of ALD that result from the mechanism of deposition described above. It is to be noted that both the characteristics of an ALD process discussed below can easily be verified experimentally (through **Figure 3. 2**).

1. *Strict thickness control:* In an ideal ALD reaction, the cyclical chemisorption of molecules results in a ML growth of film with each cycle. Thus, if a graph of film thickness is plotted with number of ALD cycles a linear curve is obtained as shown in **Figure 3. 2, left**. Extracting the slope of this curve yields the growth rate of the film (in Å/cycle). By simply controlling the number of ALD cycles, film thickness can be controlled with a fidelity which is usually $\sim 1\text{-}2$ Å.
2. *Self limiting behavior:* The ALD reaction is self limiting in nature. This implies that once all surface sites are saturated with a precursor, no further reaction can take place and hence the growth terminates. This behavior has tremendous benefits when it comes to issues of scalability and manufacturability. As compared to other thin film deposition techniques, ALD requires no target preparation (as in sputtering) or flow optimization (as in CVD) to get precise and highly uniform films. Furthermore, the dose amounts can be set at any level *past* the saturation level and highly uniform films are obtained repeatedly and at constant thickness.

The effect is easily observed experimentally by looking at growth curves as function of dose time. This is shown in **Figure 3. 2, right**. As the dose time (i.e. number of precursor molecules exposed to the substrate) increases, the thickness increases as well. However, past the saturation point no further increase in thickness is observed even though the precursor dose is increased. This indicates the surface has reached its saturation limit. Establishment of saturation curves form a true test of a reaction chemistry deposited via an ALD mechanism.

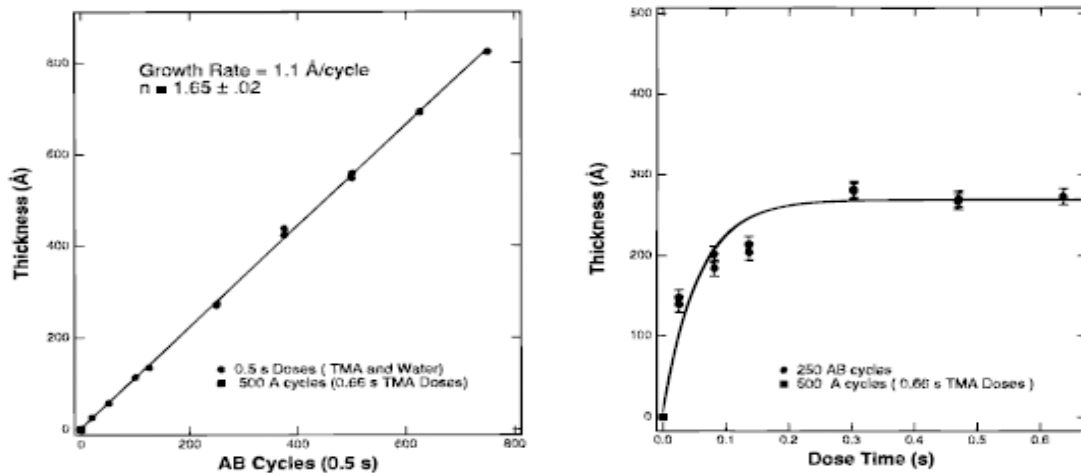


Figure 3. 2. Left graph shows linear dependence of film thickness on cycle number. The slope of the graph allows extraction of deposition rate (in Å/cycle). Right graph shows self limiting behavior of ALD films. As dose time increases, film thickness saturates indicating saturation of adsorption sites on the substrate. Data taken from George et al.^[40]

In the next two sections we will discuss, the benefits of ML control of thickness and self-limiting behavior of ALD films in developing new materials and novel applications, respectively. The formation of multicomponent nanoalloy or nanolaminate films exploits the ML control of film thickness, while the self limiting behavior allows ALD films to be deposited inside complex 3D nanoarchitectures.

Applied ALD research, I – Multicomponent films:

Researchers have exploited ALD’s ability to deposit a ML of material at a time to build binary, composite thin films. In this context, the use of the word ‘nanolaminate’ is quite widespread and perhaps a misnomer. We will distinguish composite films on their ability to maintain a single, parent phase comprising of the first film in which

the second film is homogeneously incorporated or phase separate into individual component films. The definitions of *nanoalloys* and *nanolaminates* thus follow –

1. Nanoalloys: In these multicomponent ALD films, the individual films have chemical affinity to one another. A good example of this would be Al doped ZnO films with 1-2 at% Al. Here 1 ML of Al₂O₃ is inserted after every 20 ML of ZnO. The Al³⁺ ion substitutionally dopes the Zn²⁺ sites in a ZnO parent matrix rendering it electronically conducting (n-type). This is borne out by x-ray diffraction (XRD) that can detect a decrease in the lattice parameter of the ZnO and energy dispersive x-ray spectroscopy (EDX) which can detect the right at% of Al in the ZnO film.
2. Nanolaminates: In these multicomponent ALD films, the individual films remain as separate, unmixed layers few nanometers wide, thus truly forming nanolaminates. An example of ALD-based nanolaminates would be W/Al₂O₃ films for use in x-ray optics. In this case there is little or no chemical affinity between the two materials and the two components exist as separate nanometer thin films, each imparting its own set of properties to the composite film.

An interesting variation of nanolaminates is also obtained from material systems that show alloying effects. Thus, the Al₂O₃-ZnO system can be synthesized in nanolaminate form by simply increasing the number of MLs of Al₂O₃ to be inserted after every set number of ZnO cycles. From our previous example of a nanoalloy, at% of Al in ZnO can be maintained the same, while simply increasing the number of MLs constituting the film. Thus as an extreme case, 100ML of Al₂O₃ separated by 2000ML of ZnO will still have the same at%

ZnO in the film, but the Al₂O₃ layers will form a laminate like structure separated by ZnO layers. Interesting phenomena can be studied using such material systems that may ultimately help in improving our understanding of basic atomistic processes.

A common problem during deposition of multicomponent ALD films is the interaction or ‘cross talk’ of one film with the other. Individual films that deposit at given deposition rates may behave completely differently when deposited over one another. This may be obvious to the reader, since ALD kinetics is intricately linked to the functionalization of deposition surfaces. A surface that is terminated with ligands which enhance (or hinder) chemisorption of precursors for the next pulse cycle significantly affects growth kinetics, alloying % or laminate thickness and ultimately, the properties of the composite film. As a result, there have been

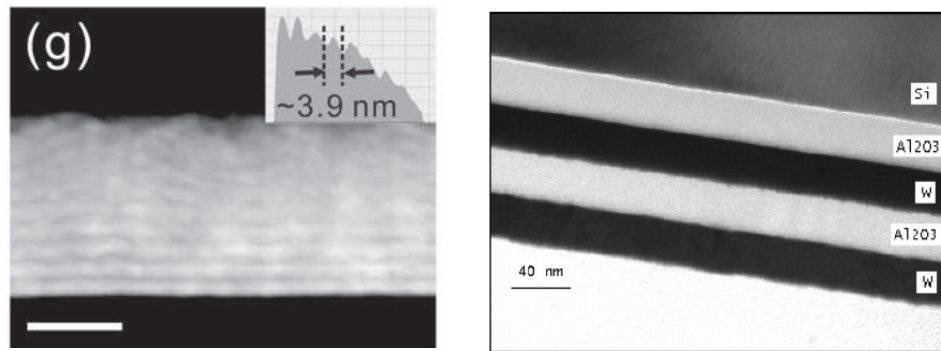


Figure 3. 3. Left, TEM cross section of a nanoalloy Al-doped ZnO film. The Al₂O₃ ML is deposited after every 19 cycles of ZnO. This corresponds to a periodicity of ~ 3.9nm.^[41] Right, TEM cross section of a nanolaminate W/Al₂O₃ film – the W and Al₂O₃ films are ~ 40nm thick and are deposited on Si substrate.^[42]

relatively few reports of multicomponent (three or more) ALD films in literature. In fact, all reported films are binary in nature, till date. A listing of the individual films along with their proposed applications is presented in **Table 3.1**.

Table 3.1 ALD-based nanolaminates in literature

	Material A	Material B	Applications	Reference
1	Al ₂ O ₃	ZrO ₂	High-k dielectrics	W. F. A. Besling, E. Young, T. Conard, C. Zhao, R. Carter, W. Vandervorst, M. Caymax, S. De Gendt, M. Heyns, J. Maes, M. Tuominen, S. Haukka, Journal of Non-Crystalline Solids 2002, 303, 123.
2	Al ₂ O ₃	ZnO	Transparent conducting oxides	J. W. Elam, Z. A. Sechrist, S. M. George, Thin Solid Films 2002, 414, 43.
3	TiN	W _x N		K. E. Elers, V. Saanila, W. M. Li, P. J. Soininen, J. T. Kostamo, S. Haukka, J. Juhanoja, W. F. A. Besling, Thin Solid Films 2003, 434, 94.
4	TiN	WN _x C _y	Barrier layer for copper metallization	K. E. Elers, V. Saanila, W. M. Li, P. J. Soininen, J. T. Kostamo, S. Haukka, J. Juhanoja, W. F. A. Besling, Thin Solid Films 2003, 434, 94.
5	Y ₂ O ₃	ZrO ₂	Solid state ionic conductor for fuel cells	C. N. Ginestra, R. Sreenivasan, A. Karthikeyan, S. Ramanathan, P. C. McIntyre, Electrochemical and Solid State Letters 2007, 10, B161.
6	Al ₂ O ₃	ZrO ₂	High-k dielectrics	D. M. Hausmann, R. G. Gordon, Journal of Crystal Growth 2003, 249, 251.
7	HfO ₂	ZrO ₂	High-k dielectrics	D. M. Hausmann, R. G. Gordon, Journal of Crystal Growth 2003, 249, 251.
8	Al ₂ O ₃	TiO ₂	High-k dielectrics	I. Jogi, K. Kukli, M. Kemell, M. Ritala, M. Leskela, Journal of Applied Physics 2007, 102.
9	Ta ₂ O ₅	ZrO ₂	High-k dielectrics	I. Jogi, K. Kukli, M. Ritala, M. Leskela, J. Aarik, A. Aidla, J. Lu, Microelectronic Engineering 2010, 87, 144.
10	Al ₂ O ₃	Ta ₂ O ₅	High-k dielectrics	Y. S. Kim, J. S. Kang, S. J. Yun, K. I. Cho, Journal of the Korean Physical Society 1999, 35, S216.
11	Nb ₂ O ₅	Ta ₂ O ₅	High-k dielectrics	K. Kukli, M. Ritala, M. Leskela, Journal of Applied Physics 1999, 86, 5656

12	Al_2O_3	ZrO_2	Ultrahigh gas diffusion barriers	J. Meyer, P. Gornn, F. Bertram, S. Hamwi, T. Winkler, H. H. Johannes, T. Weimann, P. Hinze, T. Riedl, W. Kowalsky, <i>Advanced Materials</i> 2009, 21, 1845
13	HfNO	HfTiO	High-k dielectrics	V. Mikhelashvili, G. Eisenstein, P. Thangadurai, W. D. Kaplan, R. Brenner, C. Saguy, <i>Journal of Applied Physics</i> 2008, 103.
14	Polyimide	Ta_2O_5	Dielectrics for flexible electronics	L. D. Salmi, E. Puukilainen, M. Vehkamaki, M. Heikkila, M. Ritala, <i>Chemical Vapor Deposition</i> 2009, 15, 221
15	Cr_2O_3	TiO_2	Wear resistant films	V. Sammelseg, A. Tarre, J. Lu, J. Aarik, A. Niilisk, T. Uustare, I. Netsipailo, R. Rammula, R. Parna, A. Rosental, <i>Surface & Coatings Technology</i> 2010, 204, 2015.
16	Al_2O_3	W	X-ray reflecting mirrors	Z. A. Sechrist, F. H. Fabreguette, O. Heintz, T. M. Phung, D. C. Johnson, S. M. George, <i>Chemistry of Materials</i> 2005, 17, 3475.
17	Al_2O_3	Ta_2O_5	X-ray reflecting mirrors	A. Szeghalmi, S. Senz, M. Bretschneider, U. Gosele, M. Knez, <i>Applied Physics Letters</i> 2009, 94.
18	HfO_2	TiO_2	High-k dielectrics	D. H. Triyoso, R. I. Hegde, X. D. Wang, M. W. Stoker, R. Rai, M. E. Ramon, B. E. White, P. J. Tobin, <i>Journal of the Electrochemical Society</i> 2006, 153, G834.
19	SiO_2	ZrO_2	High-k dielectrics	L. J. Zhong, F. Chen, S. A. Campbell, W. L. Gladfelter, <i>Chemistry of Materials</i> 2004, 16, 1098.
20	Er_2O_3	ZrO_2	High-k dielectrics	A. Tamm, M. Heikkila, M. Kemel, J. Kozlova, K. Kukli, V. Sammelseg, M. Ritala, M. Leskela, <i>Thin Solid Films</i> 2010, 519, 666.
21	Gd_2O_3	ZrO_2	High-k dielectrics	I. Jogi, A. Tamm, K. Kukli, M. Kemell, J. Lu, T. Sajavaara, M. Ritala, M. Leskela, <i>Journal of the Electrochemical Society</i> 2010, 157, G202.

Applied ALD research II – 3D Nanostructures

As stated before, one of the great advantages of ALD is its ability to conformally coat complex 3D nanostructures such as nanoporous low-k dielectrics,^[43] aerogels,^[44, 45] and AAO.^[46, 47] Complex inverse opal structures for photonic crystal applications have also been fabricated by fully filling the gaps between closely packed SiO₂ opals with an ALD TiO₂ film.^[48] Such superb conformality is a direct result of the self-limiting behavior in ALD chemistries. Once a surface site is saturated and given enough dose time, a precursor molecule will eventually diffuse to an empty site, deep within a porous structure. This mechanism of thin film deposition is unique to ALD only and hence ALD's widespread use in many applications which demand that functional thin films be filled into novel and complex 3D nanostructured templates. Excellent review articles summarizing research in applied ALD are already available.^[49, 50]

Currently there are two well established theories that deal with the phenomena of film conformality in high aspect-ratio (where aspect ratio is defined as the ratio of length of a pore to its diameter), 3D nanostructures. The first model is proposed by R. Gordon.^[51] In this model, a physical construct of molecules entering narrow pores is analytically solved to yield the minimum time required for complete step coverage of a pore of a given aspect ratio. However, there are two shortcomings to the model. First, the model is not a dynamic one in that it fails to take into account the fact that as the pores fill, the aspect ratio becomes more severe causing molecules to take longer times to reach the same depth inside the pore and second, the model neglects

all chemistries involved in the ALD reaction sequence. Still, the Gordon model seems to predict conformality coverage of standard chemistries quite well.^[47]

The second model is proposed by Elam et al.^[46] and is a Monte Carlo simulation of gas molecules in the molecular flow regime within the nanopores. This model predicts that there are two regimes of deposition within a nanopore. One in which the reaction chemistry is the slowest, rate limiting step and the second in which the diffusion of gas molecules is the slowest rate limiting step. The reaction chemistry is taken into account by phenomenologically tying the chemistry to a parameter termed as the 'sticking coefficient', S . By making S high or low the chemistry of the ALD process can be tuned to be highly reactive or not. Depending on which rate limiting step is dominating, the profiles of deposition will change within a nanopore. In the author's opinion, Elam's model paints a more realistic picture of the phenomena of ALD inside high aspect ratio nanostructures. The model states that both chemical as well as physical mechanisms during deposition can critically affect process parameters and that understanding ALD chemistry as well as gas diffusion dynamics are both important for successful fabrication of 3D nanostructured devices.

In the following pages, images of various structures used for ALD deposition are shown followed by a listing of ALD films, corresponding nanotemplates and possible applications with references is provided.

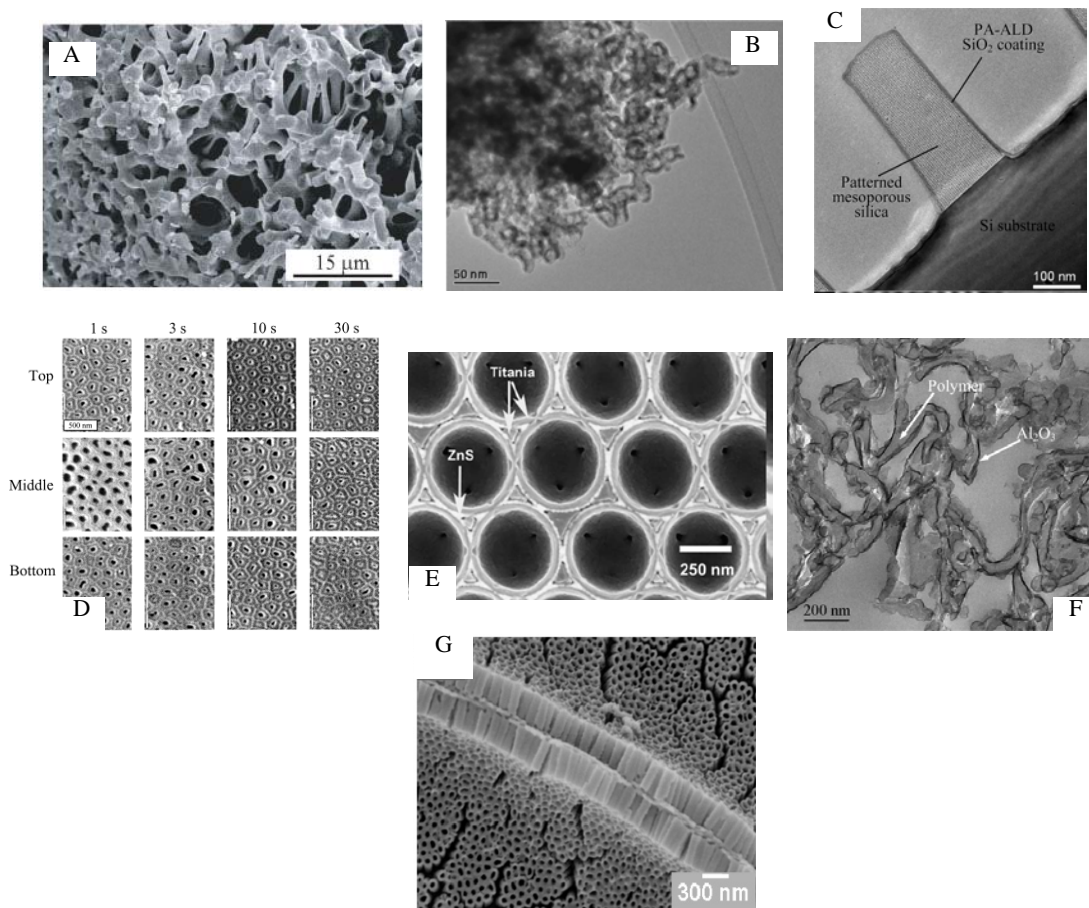


Figure 3. 4. Collection of SEM/TEM images of various ALD films deposited inside different templates A) Ru in aerogel^[44] B) W in carbon aerogel^[45] C) SiO₂ as barrier layer for mesoporous SiO₂^[52] D) ZnO at various positions inside AAO as a function of dose time^[46] E) Inverse opal structures^[48] F) polymer-ceramic composite using poly(styrene-divinylbenzene) and Al₂O₃^[53] G) TiO₂ nanorods synthesized inside AAO on flexible substrates.^[54]

	ALD Film	3D nanostructure	Purpose/Potential Applications	Reference
1	Ru	Aerogel	Catalysis of NH ₃ synthesis	J. Biener, T. F. Baumann, Y. M. Wang, E. J. Nelson, S. O. Kucheyev, A. V. Hamza, M. Kemell, M. Ritala, M. Leskela, <i>Nanotechnology</i> 2007, 18.
2	W	Carbon aerogel	Catalytic Electrodes	J. W. Elam, J. A. Libera, M. J. Pellin, A. V. Zinovev, J. P. Greene, J. A. Nolen, <i>Applied Physics Letters</i> 2006, 89.
3	Al ₂ O ₃ and ZnO	Whatman AAO	Conformality studies	J. W. Elam, D. Routkevitch, P. P. Mardilovich, S. M. George, <i>Chemistry of Materials</i> 2003, 15, 3507.
4	TiO ₂	Aerogel	Electrodes for DSSC	T. W. Hamann, A. B. F. Martinson, J. W. Elam, M. J. Pellin, J. T. Hupp, <i>Journal of Physical Chemistry C</i> 2008, 112, 10303.
	Al ₂ O ₃	poly(styrene-divinylbenzene) beads	Composite	X. H. Liang, S. M. George, A. W. Weimer, <i>Chemistry of Materials</i> 2007, 19, 5388.
5	SiO ₂	Si trench	Barrier layer for low-k ILD	Y. B. Jiang, N. G. Liu, H. Gerung, J. L. Cecchi, C. J. Brinker, <i>Journal of the American Chemical Society</i> 2006, 128, 11018.
6	TiO ₂	SiO ₂ Opals	Photonic crystals	J. S. King, D. Heine man, E. Graugnard, C. J. Summers, <i>Applied Surface Science</i> 2005, 244, 511.
7	Cu	SiO ₂ aerogels	Conformality studies	S. O. Kucheyev, J. Biener, T. F. Baumann, Y. M. Wang, A. V. Hamza, Z. Li, D. K. Lee, R. G. Gordon, <i>Langmuir</i> 2008, 24, 943.
8	MoN	AAO	Hydrophobic surfaces	V. Miiikkulainen, T. Rasilainen, E. Puukilainen, M. Suvanto, T. A. Pakkanen, <i>Langmuir</i> 2008, 24, 4473.
9	TiO ₂	AAO	Electrodes for DSSC	L. K. Tan, M. A. S. Chong, H. Gao, <i>Journal of Physical Chemistry C</i> 2008, 112, 69
10	HfO ₂	AAO	Conformality studies	I. Perez, E. Roberts on, P. Banerjee, L. Henn-Le cordier, S. J. Son, S. B. Lee, G. W. Rubloff, <i>Small</i> 2008, 4, 1223.
11	TiN-Al ₂ O ₃ -TiN	AAO	Capacitors	P. Banerjee, I. Perez, L. Henn-Le cordier, S. B. Lee, G. W. Rubloff, <i>Nature Nanotechnology</i> 2009, 4, 4.

Chapter 4: Structural, Electrical and Optical properties of ALD Al-doped ZnO Films

Abstract:

Al-doped ZnO (AZO) films of ~100nm thickness with various Al doping were prepared at 150°C by atomic layer deposition (ALD) on quartz substrates. At low Al doping, the films were strongly textured along the [100] direction, while at higher Al doping the films remained amorphous. Atomic force microscopy (AFM) results showed that Al-O cycles when inserted in a ZnO film, corresponding to a few at% Al, could remarkably reduce the surface roughness of the films. Hall measurements revealed a maximum mobility of 17.7 cm²/Vs. Film resistivity reached a minima of 4.4x10⁻³ Ω-cm whereas the carrier concentration reached a maxima of 1.7x10²⁰ cm⁻³, at 3 at% Al. The band gap of AZO films monotonically varied from 3.23 eV for undoped ZnO films to 3.73 eV for AZO films with 24.6 at% Al. Optical transmittance over 80% was obtained in the visible region. The detrimental impact of increased Al resulting in decreased conductivity due to doping past 7.3 at% is evident in the XRD data, as an abrupt increase in the optical band gap and as a deviation from the Burstein-Moss effect.

Introduction:

Since zinc oxide (ZnO) is a semiconductor material with a wide band gap of 3.27 eV and a large exciton binding energy of 60 meV at room temperature, ZnO-based thin films have been used for several applications such as transparent conducting oxide (TCO), ultraviolet light emitters, solar cell windows, and bulk acoustic wave

devices.^[55-58] Among various materials for TCO applications, Al-doped ZnO (AZO) film is a particularly attractive material because of its excellent properties, such as higher thermal stability, good resistance against damage by hydrogen plasma and low cost of fabrication, compared to indium tin oxide (ITO).^[59] Therefore, a number of fabrication techniques such as sputtering,^[56, 57] pulsed laser deposition (PLD)^[58] and chemical vapor deposition (CVD)^[60] have been adopted to deposit AZO thin films.

On the other hand, the reduction of thin films to nanometer dimensions for new technologies requires precise control of film thickness, conformality, and morphology. For example, a lower deposition temperature is also required for deposition onto plastic substrates for flexible electronics and to minimize interlayer diffusion in nanoscale devices. These requirements can be achieved by an atomic layer deposition (ALD) technique which can realize film growth controlled to within a single atomic layer by means of a binary reaction sequence chemistry.^[61]

Past work on ALD-based AZO films has involved studying the structural, morphological and electrical properties of AZO films across the entire composition spectrum.^[62-64] However, optical characterization which may yield band gap information of these films have not been evaluated. Hall measurements which provide complete information on conduction characteristics including resistivity, mobility and carrier concentration is also lacking. Both these measurements are important as they provide a physical and atomistic view of the effect of Al doping in ZnO grown via ALD. Therefore, in this study AZO films were deposited at a low temperature of 150°C by the ALD method and then systematically analyzed for its structural, electrical and optical properties which included optical characterization and Hall

measurements. We fabricated Al-doped ZnO thin films with various Al doping concentrations by inserting an Al₂O₃ ALD cycle after every 'n' ZnO cycles, varying n from 40 to 5, to achieve different ZnO/Al₂O₃ ratios. Since there are only a few reports on low temperature, ALD ZnO-based films prepared by the ALD technique,^[62-66] this work adds valuable information on the structure-property relationship in ALD-based AZO films.

Experimental:

AZO thin films were deposited at 150°C using a BENEQ TFS-500 ALD viscous-flow reactor. An example of the recipe syntax is provided in the appendix. High purity quartz glasses were used as the substrate for AZO film growth. Diethyl zinc (DEZ, Zn(C₂H₅)₂) and distilled (DI) water were used as precursors to deposit ZnO films at a growth per cycle (GPC_{ZnO}) of 0.2 nm/cycle. Pulse times for DEZ and DI water cycles were kept at 250ms. High purity nitrogen was adopted as a purging gas. For preparing ALD-Al₂O₃ films at 150°C, trimethyl aluminum (TMA, Al(CH₃)₃) and DI water were used as precursors at a GPC_{Al₂O₃} of 0.1 nm/cycle. Pulse times for TMA and DI water cycles were kept at 250ms. The GPC for ZnO and Al₂O₃ was established during deposition of pure, individual ZnO and Al₂O₃ ALD films respectively, in each case the process recipe achieving the characteristics (uniformity, precursor dose saturation, etc.) expected for ALD.

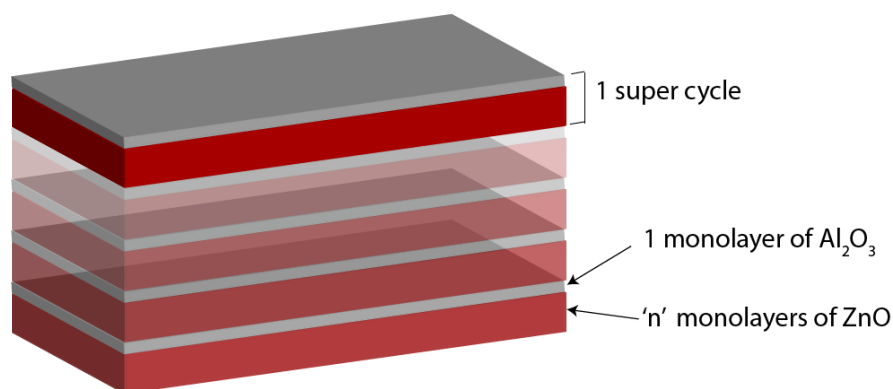


Figure 4. 1. Schematic diagram of the film stack used to make various Al-doped ZnO films by atomic layer deposition.

To achieve a particular at% Al doping into ZnO films, a single TMA-DI water cycle was inserted after a set number of DEZ-DI water cycles. This constituted one ‘super-cycle’ of AZO, composed of n cycles of DEZ-DI water followed by one cycle of TMA-DI water. **Figure 4. 1** shows the schematic diagram of the film stack used to make various AZO films by the ALD method. Here ‘n’ was varied from 40 to 5 to produce various compositions of AZO films. The super-cycles were calculated to target a resultant thickness of ~100 nm for each AZO film. Thickness of the films were measured using spectroscopic ellipsometry (Sopra GES5E) and optical models discussed elsewhere.^[67] An x-ray diffractometer (X’pert MPD, Panalytical, 40 kV, 30 mA) was used to investigate structural properties of the thin films. EDX was done on a Hitachi SU70 SEM using a Bruker Silicon Drift Detector attached to the SEM column with a beam energy of 20 keV. The surface morphologies of the thin films were investigated by a scanning probe microscope (SPM) in the atomic force microscope (AFM) mode (SPA-400, Seiko Instruments). The electrical properties of the thin films were measured by van der pauw method at room temperature using a

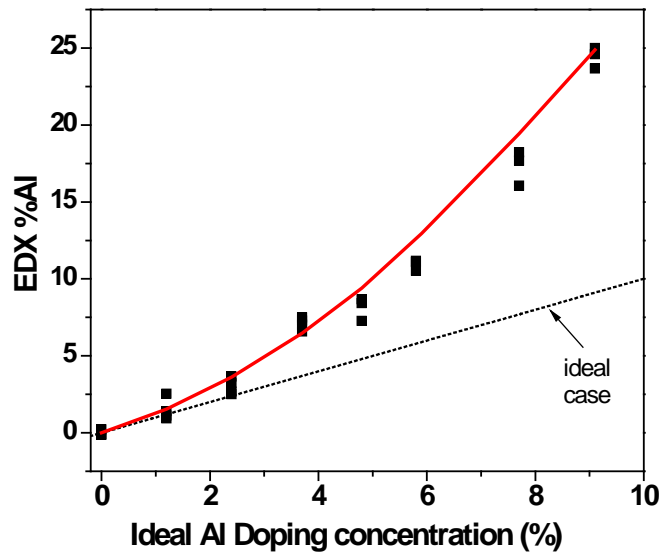


Figure 4. 2. Variation of true at% Al in AZO films measured via EDX with the

ideal at% Al calculated as
$$Ideal\ at\% Al = \frac{GPC_{Al_2O_3}}{GPC_{Al_2O_3} + nGPC_{ZnO}}$$
 due to the

processing sequence adopted for doping the AZO films. The dashed line shows, in the ideal case, that true at% Al should be equal to the ideal at% Al. The fit (solid) is a phenomenological fit to the data and is described in text.

Hall Effect measurement system (Ecopia HMS 3000). A spectrophotometer

(Shimadzu RF-1501) was used to measure the transmittances of the thin films in the wavelength range of 250–900 nm.

Results and Discussion:

Phenomenological model for at% Al doping:

The thickness of the films was found to be off-target for the higher at% Al samples.

Similarly, the ideal at% Al given by $\text{Ideal at\% Al} = \frac{\text{GPC}_{\text{Al}_2\text{O}_3}}{\text{GPC}_{\text{Al}_2\text{O}_3} + n\text{GPC}_{\text{ZnO}}}$ was found to

deviate at higher at% Al samples as well. This is verified using EDX and is presented in **Figure 4. 2**. For instance, in case of the AZO film grown with $n=10$, the target thickness was calculated to be 100.1 nm and the ‘ideal’ at% Al was 4.8%. However, the true thickness was found to be 96.8 nm and a true at% Al of 8.1% was obtained for this sample using EDX. It is known that ZnO encounters barrier to growth on Al_2O_3 and thus both thickness and at% Al are affected in these samples.^[63] Henceforth, at% Al will be given in terms of true at% Al as determined by EDX. No post-deposition, thermal annealing was performed.

To phenomenologically model the suppressed growth of ZnO on Al_2O_3 , it was assumed that the areal density of Zn atoms as a result of reduced adsorption of DEZ on Al_2O_3 follows an exponential behavior given by $\rho_{\text{Zn}} = \rho_{\text{Zn}}^0 (1 - \exp(-\frac{n}{\tau}))$ where, ρ_{Zn}^0 is the ideal, areal atomic density of Zn in ZnO, ‘n’ is the n^{th} cycle number after Al_2O_3 deposition and τ is the cycle number required for ρ_{Zn} to reach 63.2% of ρ_{Zn}^0 - the ideal areal density. This assumption is valid since it is expected that after a thick enough layer of ZnO is deposited on Al_2O_3 the GPC for ZnO will be close to that observed in pure ALD ZnO films. Thus, this analysis quantifies the kinetics of the recovery behavior of ZnO deposition. Since only one cycle of Al_2O_3 is used for

alloying, we assume that the areal atomic density of Al in Al₂O₃ is constant across all the samples and, for simplicity, is equal to the equilibrium value found in pure Al₂O₃. Using the planar atomic density of Zn in ZnO given by $\rho_{Zn}^0 = 8.34 \times 10^{14} / \text{cm}^2$ and Al in Al₂O₃ as $\rho_{Al}^0 = 4.44 \times 10^{14} / \text{cm}^2$,^[62] the at% Al can be modeled by simply integrating the atomic density dependence on cycle number, as given above, to obtain

$$\text{at\% Al} = \frac{100}{\left[\frac{\rho_{Zn}}{\rho_{Al}} \left(n - \tau + \tau \exp\left(-\frac{n}{\tau}\right) \right) \right] + 1}$$

and comparing it with the EDX data. From this

equation, the value of τ is found to be ~ 6 and is shown in solid in **Figure 4. 2**. Thus, it takes approximately 6 cycles of ZnO to recover 63.2% of its original atomic areal density when depositing on a single monolayer of Al₂O₃. The recovery behavior given by $\tau \sim 6$ is expected to change if more than one monolayer of Al₂O₃ is used in alloying.

X-ray Diffraction Data:

The structural properties of the films were analyzed next. **Figure 4. 3** shows X-ray diffraction patterns for AZO films prepared varying ‘n’, the number of DEZ-DI water cycles inserted for every TMA-DI water cycle. The crystalline state and crystal orientation of the as-deposited films were found to change with ‘n’. ZnO films grown without any TMA-DI water cycle exhibited a polycrystalline state having (100), (002), (101) and (110) orientation. However as Al₂O₃ is introduced, the (002) peak disappears and the intensity of the (100) peak becomes dominant reaching a maximum at $n = 20$. With further decrease in ‘n’ i.e., increased Al doping, the (100)

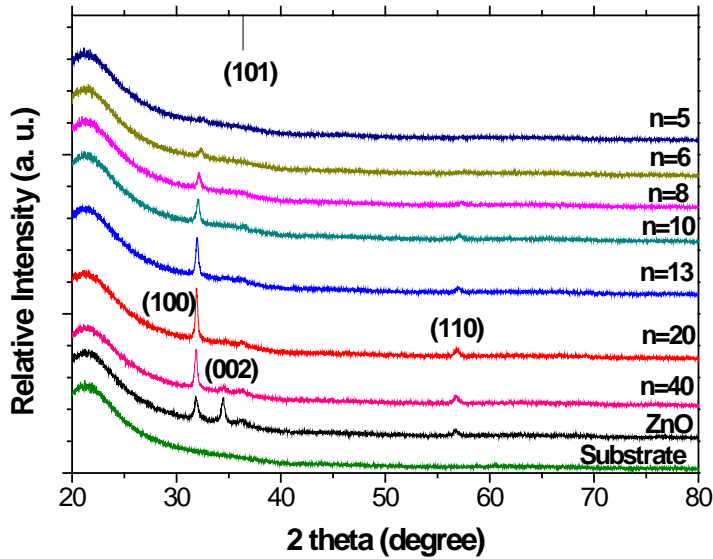


Figure 4. 3. X-ray diffraction patterns for Al-doped ZnO films prepared by different cycle combination, where n is the number of DEZ-DI Water cycles separated by two TMA-DI Water Cycles. Lower the n, higher the at% Al doping.

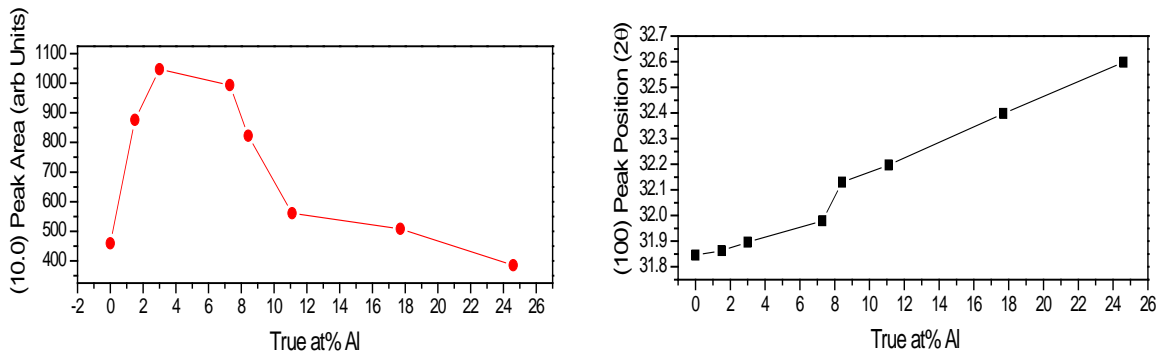


Figure 4. 4. Left - Area under the (100) peak for Al-doped ZnO films with different Al concentration. The peak areas have been normalized with respect to at% Zn and thickness of the films. The area maximizes at 3.0 at% Al (shown by the arrow). Right - Peak position of the (100) as a function of at% Al. There is a kink in the linear trend observed at 7.3 at% Al.

peak diminishes in intensity and at $n=5$ no peak is observed, which indicates that the AZO film at 24.6 at% Al is amorphous.

The area under the (100) peak is plotted in **Figure 4. 4, left**. Because the films have various thicknesses, care has to be taken to interpret the results since crystallization behavior is often thickness dependent. In our case, the area of the (100) peak is normalized to the amount of Zn present in the individual films. This is done by using the ratio of Zn:Si peaks from the EDX data obtained earlier for films deposited on quartz substrates (see Supplemental Section S1). For a constant composition, thinner films will have a lower Zn:Si ratio than thicker films. Similarly, for a constant thickness higher at% Zn films will have a higher Zn:Si ratio. Thus, the EDX Zn:Si ratio provides a convenient method to normalize data where thickness and composition are convoluted with one another. As stated before, the area of the (100) peak goes through a maxima at 3 at% Al ($n= 20$) and then decreases subsequently. It is well known that the [002] direction i.e. the c-axis, is the preferential orientation commonly observed in ZnO and doped ZnO films prepared by various deposition techniques such as sputtering, PLD and CVD.^[67-69] However, ALD processes have been shown to yield a texturing effect which is dependent on temperature, pulsing and purging times.^[65, 70, 71] The [100] orientation i.e. the a-axis, is found to occur in a narrow temperature window that spans from 155-220°C and has been attributed to the breakdown of negatively charged hydrocarbon ligands in DEZ which disturb the charge distribution on (002) planes.^[70]

In the current scheme however, it was found that [100] direction is dominant when Al^{3+} is introduced as a dopant. To explain this behavior, it is worthwhile to note

that the (002) plane consists of alternate planes of Zn^{2+} and O^{2-} and thus is charged positively or negatively respectively, depending on surface termination. On the other hand, the (100) plane is a charge neutral surface consisting of alternate rows of Zn^{2+} and O^{2-} ions on the surface. Thus, it is conceivable that the layer-by-layer growth during ALD may cause the Al^{3+} ions to disturb the charge neutrality of the (100) plane thereby affecting its surface energy and causing its preferential growth. Indeed, it has been reported^[64] that an exchange reaction between TMA and the ZnO surface is possible. This may lead to texturing effects in the films not found in other modes of deposition or growth.

The (100) peak position is plotted in **Figure 4. 4, right**. The peak position increased with increasing Al concentration in AZO films – linearly with doping with a ‘kink’ at ~7.3 at% Al. This implies that Al addition into ZnO film reduces the d-spacing along the [100] direction. We attribute this to Al^{3+} ions substitutionally doping the Zn^{2+} at random sites. The Zn^{2+} ionic radius is 72 pm compared to the Al^{3+} of 54 pm and could thus result in smaller interplanar distances.^[72] Recently, Yoshioka et al.,^[73] have studied the ZnO- Al_2O_3 system and concluded that a stretching along c-axis occurs past 8 at% Al as well. This has been attributed to the presence of a metastable, homologous phase where the Al^{3+} ion has a coordination number (CN) of 5 even though it resides on a Zn^{2+} site (CN = 6). Since their films were c-axis oriented no information on the d-spacing along the a-axis were provided but it is conceivable that the stretching along the c-axis along with a smaller Al^{3+} ionic radius can cause a decrease in the d-spacing along the [100] direction. The issue of metastable phase formation will be touched upon again while discussing the correlation between

structural, electrical and optical properties. The presence of a spinel ZnAl_2O_4 phase can be ruled out since it occurs at a lower 2θ than the (100) peak in the XRD profile.^[74] The absence of the spinel phase in ALD AZO films have been reported by Elam et al. as well.^[63]

AFM and Surface Roughness:

The surface morphologies of the thin films with a scanning area of $2\ \mu\text{m} \times 2\ \mu\text{m}$ were analyzed by using a SPM in the AFM mode. **Figure 4. 5** shows the root mean square (rms) surface roughness for AZO thin films as a function of at% Al.

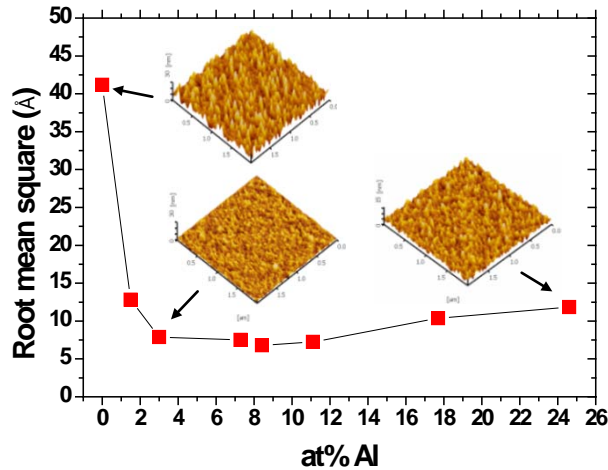


Figure 4. 5. The rms roughness and associated surface morphologies obtained via AFM for Al-doped ZnO films as a function of at% Al.

AFM images of three representative films - pure ZnO, n=20 (3 at% Al) and 5 (24.6 at% Al) is also shown in the inset of the figure. It is found that the surface roughness is strongly dependent on at% Al. The roughness of ZnO films grown without the TMA-DI water cycle was 4.1 nm and then dramatically decreased with increasing Al doping. As the at% Al reached over 3.0%, the rms roughness values of AZO films

saturated to around 0.8 nm and then slightly increased to 1.0~1.1 nm for over 17.3 at% Al. This AFM result shows that even a single cycle of TMA-DI water separated by 40 cycles of DEZ-DI water can remarkably reduce the roughness of AZO films. Similar results have been reported by Elam et al., for nanolaminate Al₂O₃-ZnO films and is attributed to the Al³⁺ ions substituting surface Zn²⁺ ions thus stymieing ZnO crystal growth.^[64] The slight increase in the roughness at higher at% Al has been attributed to TMA etching of the ZnO surface, although we find no evidence of the sudden increase in rms roughness at similar at% Al as reported by Elam et. al.^[62] Perhaps the discrepancy lies in the difference in analysis techniques used to determine at% Al in the films. Whereas the present study uses EDX, Elam et al., have used inductively coupled plasma atomic emission spectroscopy (ICP-AES) to determine Al doping in the films. Notwithstanding this, the roughness results highlight AZO's potential use as a TCO, especially where low temperature and precise control over film uniformity, smoothness, conformality and thickness is required.

Hall Measurements:

Hall measurements were carried out at room temperature to investigate the electrical properties of AZO thin films. This is shown as a function of at% Al in **Figure 4. 6**. Note that all the films, both AZO and pure ZnO, were n-type semiconductors. In the case of pure ZnO film, the carrier concentration and the mobility were $1.0 \times 10^{19} \text{ cm}^{-3}$ and $17.7 \text{ cm}^2/\text{V}\cdot\text{s}$, respectively. As the Al doping increased, the carrier concentration of AZO films at first increased rapidly and then saturated to $\sim 1.7 \times 10^{20} \text{ cm}^{-3}$. For Al doping over 11 at%, the carrier concentration of AZO films was abruptly reduced. The mobility of AZO films continuously decreased from 17.7 to $0.2 \text{ cm}^2/\text{V}\cdot\text{s}$ while Al

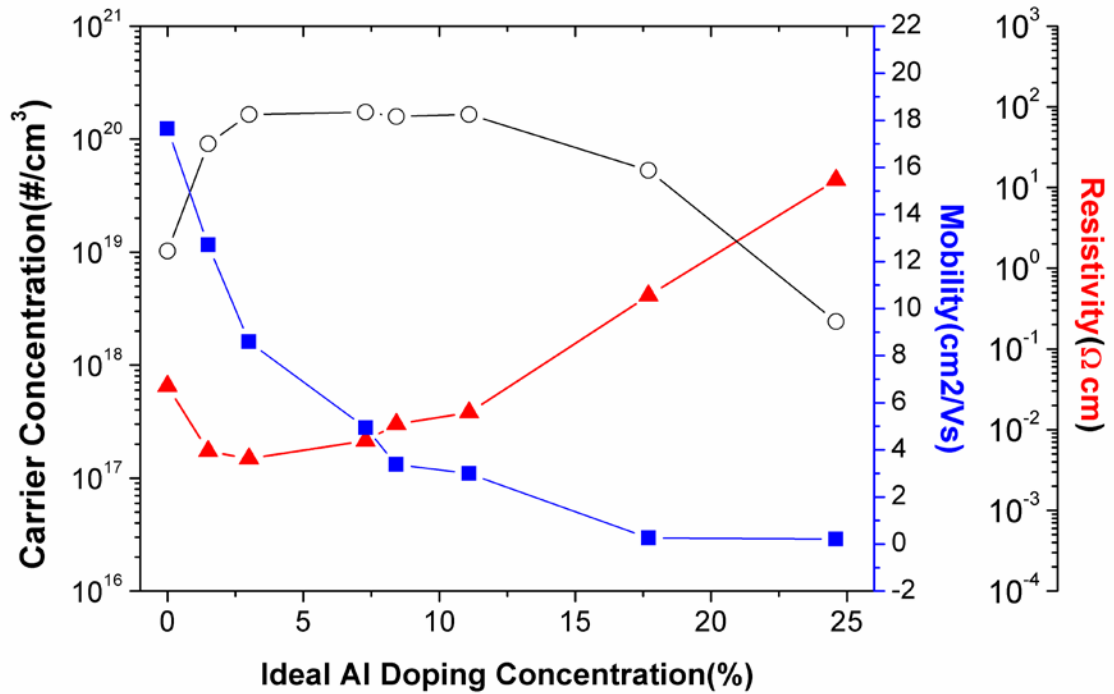


Figure 4. 6. Room temperature carrier concentration (-○- left axis), mobility (-■- right axis) and resistivity (-▲- right axis, offset) as a function of at% Al doping for AZO films.

doping increased from 1.5 to 24.6 at%. Furthermore, the lowest resistivity of $4.4 \times 10^{-3} \Omega\text{-cm}$ was obtained for AZO films grown with 3.0 at% Al ($n = 20$). This resistivity value is higher than those reported for AZO films from other deposition processes. However, note that the films are only ~100 nm thick, whereas past work has focused on films with higher thicknesses. Furthermore, the lowest resistivity is obtained at an AZO composition of 3 at% Al which is in line with prior reports, e.g., Hüpkes et al., report a minimum resistivity ($2.4 \times 10^{-4} \Omega\text{-cm}$) for 700-900 nm AZO films at 3 at% Al.^[75] Further increase in at% Al increased the resistivity. Interestingly, the 3.0 at% Al sample also showed the highest XRD (100) area under the peak and the lowest surface roughness, indicating that both the degree of crystallinity and surface roughness play an important role in determining the resistivity of AZO films. These

results are consistent with Matthiessen's rule for electrical conductivity which takes into account contributions to resistivity from thermal vibrations (i.e., phonons), impurities and defects.^[76] Thus, highly crystalline films with smoother surface morphology would lead to less carrier scattering, higher mobilities and therefore, improved conductivity. Similar results linking conductivity to grain morphology are reported by Lu et al., who report a maxima in the grain size and a minima in resistivity at 4.0 at% Al for sputtered AZO films.^[77]

Optical Properties

For TCO application, the transmittances (T) of AZO thin films were measured at room temperature by a double-beam spectrophotometer. The transmittance spectra for various samples is shown in **Figure 4. 7, left** in the wavelength range of 250–900 nm.

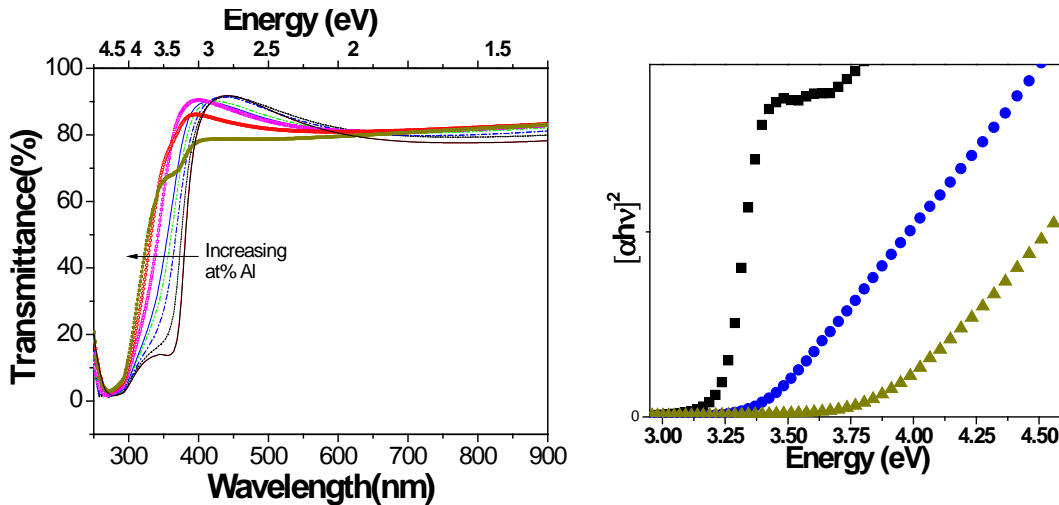


Figure 4. 7 Left, transmittance as a function wavelength (bottom x-axis) and energy (top x-axis) for various Al concentrations in AZO films. The absorption edge blue-shifts for higher at% Al doping. Right shows Tauc Plots for three representative samples - ■ for 0 at% Al, ● for 7.30 at% Al and ▲ for 24.6 at% Al.

All of the thin films prepared with various Al doping levels showed as high as 80~92% optical transmission in the visible range, which is important for TCO applications such as solar cell windows. The band gap of AZO thin films can be measured by fitting the sharp absorption edges. In order to calculate the band gap energies of the thin films, Tauc plots were drawn where it was assumed that the absorption coefficient $\alpha \sim -\ln(T)$ corresponding to the direct band gap of the wurtzite structure of ZnO. A plot of $[\alpha \times (h\nu)]^2$ against the photon energy ($h\nu$) was drawn and the sharp absorption edge could be accurately determined for the thin film by the linear fit (**Figure 4. 7, right**). The absorption edge undergoes a blue shift with increasing Al doping.

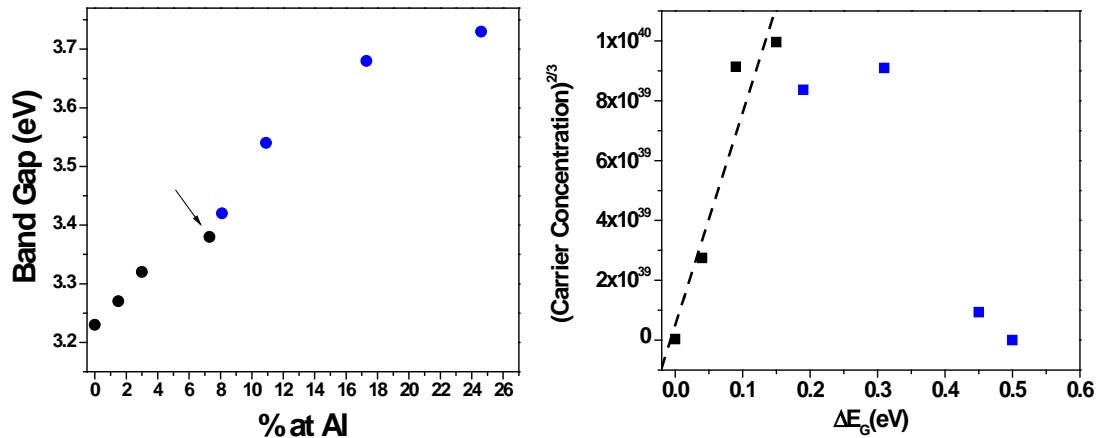


Figure 4. 8. Left, bandgap as a function of Al concentration for Al-doped ZnO films prepared with different Al doping concentration. The arrow shows at % Al beyond which band gap increases rapidly. Right, the relationship between (carrier concentration)^{2/3} and the bandgap change, ΔE_G . The linear trend is due to the Burstein-Moss effect which occurs till ~7.3 at % Al.

Analysis and Discussion:

To understand the increase in the energy of the absorption edge with Al doping further, the optical band gap energies are plotted with at% Al in Figure 8a. It was observed that the optical band gap of AZO thin films changed from 3.23 to 3.73eV for Al doping varying from 0 to 24.6 at%, respectively. The ideal band gap of pure ZnO is 3.27eV and that of Al₂O₃ is 8.7eV.^[55, 78] Thus, the increase in bandgap is to be expected with increase in at% Al. However, the band gap of AZO increases abruptly at ~ 7.3 at% Al. This corresponds to the kink observed in the XRD peak position (Figure 4b), providing further indication that at low at% Al, Al³⁺ ions substitutionally occupy the Zn²⁺ sites and perturb the properties of pure ZnO. However at higher at% Al, three scenarios are possible a) phase segregation of Al from ZnO b) formation of a spinel ZnAl₂O₄^[74] or c) formation of a metastable (ZnO)₃(Al₂O₃) phase.^[73] Al phase segregation in a ZnO matrix would result in increased conductivity of the resulting film. Since electrical data does not support this fact and no sign of a spinel-like phase in XRD is detected, the discontinuities observed in XRD and optical data and the loss in carrier concentration most likely stem from the presence of the metastable phase as predicted by Yoshioka et al.'s work.^[73] The low temperature of deposition and ALD's monolayer-by-monolayer growth mechanism may result in formation of thermodynamically metastable phases. It should also be noted that the thickness of the AZO films (~100 nm) in this work is one of the thinnest studied and the resultant stress and high interface/surface to volume ratio in these films may play a role in energetically favoring the nucleation and growth of such a phase as well.

Finally, the increase in band gap observed in TCO's is normally believed to be due to the Burstein–Moss effect.^[79, 80] This effect has been well characterized for AZO films^[77, 81-83] and can be explained as follows - since ZnO thin film is naturally n-type, addition of donor Al³⁺ ions raises the Fermi level of AZO films into the conduction band making the films completely degenerate and hence the absorption edge shifts to energies higher than the actual band gap of the material. Ignoring many-body effects,^[84] since carrier concentrations in all the samples were $\sim 10^{20} \text{ cm}^{-3}$ and lower, the Burstein-Moss model predicts a $N^{2/3}$ (carrier concentration obtained from Hall measurements) dependency of ΔE_G (the difference between the measured bandgap of AZO films and the bandgap of the pure ZnO thin film in this work). Such a plot of $N^{2/3}$ vs. ΔE_G is shown in Figure 8b. A linear trend is only observed until at% Al of 7.3%. Beyond this value of doping, the carrier concentration does not depend linearly on the substitutionally doped Al³⁺ ions anymore, indicating a change in the mechanism and reduction in formation of free charge carriers. This trend seems consistent with the XRD, electrical and optical data.

The results in this paper demonstrate certain characteristics of ALD-based AZO films as compared to currently established methods of deposition. Firstly, ALD can easily be used to dope ZnO and other oxide films by simply changing the sequence of precursor pulses. No target preparation (as in sputtering or PLD) or flow optimization (as in CVD) are required to get precise and highly uniform films. Secondly, ALD provides a unique tool to manipulate crystallographic orientation of AZO films. As shown in the past, this can be done by varying temperature pulse and purge times. In this paper, we show that a similar effect can be achieved with doping ZnO films as

well. Thirdly, given the low temperature of deposition and the ability of ALD to place monolayers of disparate materials contiguously to one another, many metastable phases could be accessed which may be harder to obtain using previously demonstrated deposition processes. Finally, given these characteristics of ALD-based AZO films, it is interesting to note that the film is optimized for resistivity at the same at% Al as reported largely in literature.

Conclusion

Al-doped ZnO thin films of 100 nm thickness were prepared by systematically changing the number of DEZ-DI water cycles inserted between two TMA-DI water cycles at 150°C by an atomic layer deposition (ALD) method. Whereas, pure ZnO film was polycrystalline, the AZO films crystallized preferentially along the [100] direction as a result of doping with Al. A single TMA-DI water cycle could remarkably reduce the roughness of ZnO films, highlighting its potential use for TCO based applications. The lowest resistivity of $4.5 \times 10^{-3} \Omega\text{-cm}$ was observed for AZO films ~ 100nm thick and grown with 3.0 at% Al doping concentration (i.e., with 20 DEZ-DI water cycles for every single TMA-DI water cycle). Transmittances of over 80% were observed in the visible region for the films. The band gap of AZO increased with increasing Al doping concentration. However, the Burstein–Moss effect is only responsible for increase in the band gap until about 7.3 at% Al.

It was found that at low at% Al doping (7.3 at% Al and lower), AZO films behave as substitutionally-doped TCO, where the properties of the ZnO are perturbed due to the presence of Al^{3+} ions on Zn^{2+} sites. This results in AZO films with a high degree of crystallinity, low resistivity and an increase in band gap consistent with the Burstein-

Moss effect. At higher at% Al (8.1 at% and higher), structural, electrical and optical properties indicate the formation of a possible metastable phase as predicted in a recent published work.^[73] This effect is manifested in the AZO films as a decrease in crystallinity, an increase in resistivity and deviation from the Burstein-Moss effect.

Chapter 5: Atomic layer deposition of p-V₂O₅.nH₂O for rectifying p-V₂O₅/n-ZnO diodes

Abstract:

We demonstrate high current rectification in a new system comprising of 30nm of hydrated vanadium pentoxide and 100nm of zinc oxide (V₂O₅.nH₂O–ZnO) thin film structures. The devices are prepared using a low temperature (<150°C), all atomic layer deposition process. A surprising element is that the rectifying behavior arises from p-type conductivity in V₂O₅ – an otherwise well known n-type semiconductor. Experimental evidence points to protonic conductivity due to intercalated water in V₂O₅ as the source for p-type behavior. The diode characteristics are strongly dependent on the electrode material in contact with V₂O₅.nH₂O. A high I_{on}/I_{off} ratio (598) at ± 2V is obtained for oxygen-free Pt electrodes, whereas a low I_{on}/I_{off} ratio (19) is obtained for oxygen-rich ITO electrodes, suggesting the deleterious effects of oxygen atom reactivity to device characteristics.

Introduction:

Metal oxide (MO) based semiconductors form a large class of oxide materials that exhibit a fascinating variety of electrical properties. To a first approximation, these properties are related to the band gap (E_g) of the semiconductor which varies from 1eV to 3.5eV in most MO semiconductor systems. The E_g in turn, depends strongly upon the chemistry i.e., the ionicity and strength of the metal-oxide bond. Point defects such as vacancies and dopant atoms play a crucial role in fine tuning the band

structure and carrier concentration in these materials. Recent advancements in the understanding of these materials have led to the successful integration of MO semiconductors in many modern devices such as photodetectors,^[85] gas sensors,^[86] catalysts,^[87] transistors^[88] and photovoltaic devices.^[89]

A prerequisite to engineer electronic devices is the ability to manipulate and modulate the charge carrier concentration in materials. While this is easily achieved in n-type MO semiconductors under ambient conditions via oxygen vacancies and donor atoms, the problem of finding a p-type MO semiconductor system has been elusive.^[90] Amongst naturally occurring MOs, only NiO and Cu₂O are known to be p-type.^[91, 92]

Thus, due to the lack of simple p-type oxides, there are relatively few reports of oxide based devices such as diodes and transistors which are the simplest, yet essential building blocks for complex electronic circuits.^[88, 93] The devices produced to date can be categorized into two broad classes based on the type of p-type material used. First, devices which utilize a simple p-type metal oxide such as NiO^[91, 94-96] and Cu₂O^[97-102] and second, devices which employ more complex, binary^[103, 104] (eg., p-SrCu₂O₂, CuAlO₂) and ternary oxides^[93] (eg., InGaZnO₄) for the p-type material.

In this paper, we present the diode behavior of a new material system - hydrated V₂O₅ (V₂O₅.nH₂O) and ZnO, both deposited using low temperature (<150°C) atomic layer deposition (ALD), thus adding to the list of metal oxides which can be used for diode fabrication. ALD is a cyclical, self-limiting surface reaction controlled thin film deposition technique that leads to superb control over thickness and uniformity.^[34] Whereas it is known that ZnO is n-type,^[7] the p-type behavior we report from an

ALD process is particularly surprising for V_2O_5 , since these films have always been reported to be n-type.^[105-107] However, Livage and co-workers have shown that when V_2O_5 is intercalated with water, protonic (H^+ or H_3O^+) conduction is possible.^[106] Incorporation of water species is credible in ALD because of the use of water as a precursor and because deposition temperatures are low, potentially suppressing desorption of water-related reaction products. We believe therefore that the V_2O_5 layers behave primarily as p-type ionic conductors while the ZnO layers serve as n-type electronic conductors. The p-type behavior in V_2O_5 is realized by the room temperature aging process that the films undergo as part of our device processing scheme.

Experimental Details:

Device Fabrication:

In this section, we describe the procedure for making pn junctions on ITO glass electrodes. The same process was replicated for making devices on other electrodes as well. ITO glass substrates were obtained from Delta Technologies Inc. The sheet resistance of the ITO layer was determined to be 4-8 Ω/\square with a nominal thickness of 150nm. The substrates were degreased in an ultrasonic bath containing acetone solution, washed in de-ionized water (DIW) and blown dry with compressed air. A small region of the substrate was then masked with a dry erase marker. This masked region ultimately serves as the bottom contact during electrical testing of the devices. ALD V_2O_5 films were then deposited on this substrate in a BENEQ TFS 500 reactor set to a temperature of 120°C. The vanadium precursor used was vanadyl triisopropoxide (VTOP) while DIW served as the oxidant.^[108] A pulse/purge cycle of

0.5s/1s and 2s/1s was used for the VTOP and DIW, respectively. The growth per cycle (GPC) for V_2O_5 was determined to be $0.3\text{\AA}/\text{cy}$ – in line with reported values^[109] and cross wafer uniformities across a 4" Si wafer were better than 95%.

For preparation of pn junction devices, the thickness of V_2O_5 was chosen to be $\sim 30\text{nm}$. The film was then aged in a controlled, ambient laboratory environment (25°C and relative humidity of 45%) for at least two days before reentering the ALD chamber for ZnO deposition. We found the two day period to be necessary and ample to induce p-type behavior in V_2O_5 . Longer wait periods did not impact device characteristics significantly.

ALD ZnO films were deposited using diethyl zinc (DEZ) and DIW. A target thickness of 100nm was used. The temperature of the deposition process was kept at 150°C . The pulse times used were 0.25s/0.5s for both DEZ and DIW. A GPC of $2\text{\AA}/\text{Cy}$ was determined for this process, in line with published values.^[64] Uniformities across 4" Si wafers were better than 95%. It has been verified using XRD (not shown) that the deposited ZnO film is crystalline and in the wurtzite phase.

For top electrode fabrication, Au was sputtered using a Denton Standard Desk III sputtering system through shadow masks creating circular dot electrodes with two diameters measuring $125\mu\text{m}$ and $250\mu\text{m}$ respectively. Finally the dry erase marker tab was removed from the sample using acetone. This re-exposed the bottom electrode ITO for bottom contacting the device during electrical measurements.

Samples and Equipment for Characterization:

Besides substrates with conducting BE, Si and quartz substrates were also used to characterize the V_2O_5 and ZnO films for their optical and structural properties. For

various tests described below, the thicknesses ranged from 30nm-100nm for V_2O_5 and ZnO films. FTIR was done on a Thermo Nicolet Nexus 670. XRD was done on a Bruker D8 Advance system. Thickness measurements were performed using the GE5 spectroscopic ellipsometer (SE) from SOPRA. Electrical measurements were performed on a fully automated home-built probe station with auto XYZ controls and a microscope with a 10X objective lens for accurately measuring electrode diameters after Au sputter deposition through the shadow mask. All current voltage (IV) measurements were made using a Keithley 2400 series source measure unit (SMU) while capacitance voltage (CV) measurements were carried out using an Agilent LCR E4980A meter using customized and automated Labview™ programs. Hall measurements were performed on an ECOPIA HMS 5000 Hall Measurement Unit. Van der Pauw structures were made for Hall measurements. To prepare these structures, In-Sn contacts were melted at the four corners of precisely cut 1cmx1cm high purity quartz substrates (0.5 mm thick) coated with the film of interest (V_2O_5 or ZnO).

Results:

V_2O_5 Film Structure:

First, we performed FTIR spectroscopy on fresh and aged V_2O_5 films. These data are shown in **Figure 5. 1**. As the film ages, a broad absorption peak forms around 3600-3100 cm^{-1} with shoulders on both sides. The shoulders are attributed to the vibrations characteristic of intercalated H_2O in V_2O_5 , particularly, the H_3O^+ vibration at 3200 cm^{-1} and the OH^- vibration at 3581 cm^{-1} .^[110] For the purpose of this paper, we

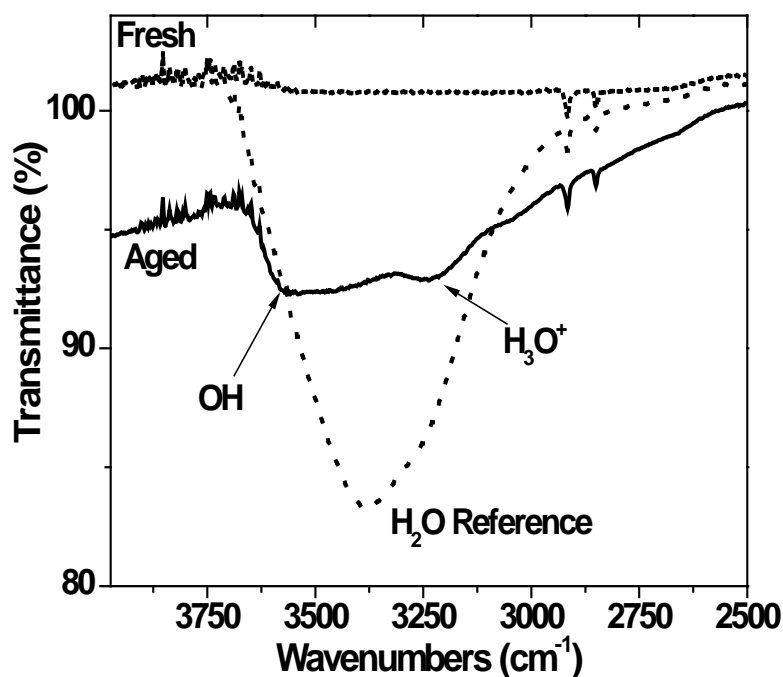


Figure 5. 1. Part of the FTIR spectrum obtained from fresh, aged films and reference sample for H₂O. The water-related absorption in the aged film is clearly seen in the broad peak observed from 3100-3600cm⁻¹. The shoulders in the aged film correspond to OH and H₃O⁺ vibrations.

will denote adsorbed water and related species in V₂O₅ as H₂O only. Where needed, we will distinguish H₃O⁺ from H₂O as the species responsible for protonic conduction. For comparison, the spectrum for pure water consists of a broad peak at 3300 cm⁻¹ and is also show in **Figure 5. 1**. Thus, aging of the ALD V₂O₅ film causes H₂O adsorption in the film. This adsorbed H₂O is intercalated into the V₂O₅ film structure as explained below.^[106]

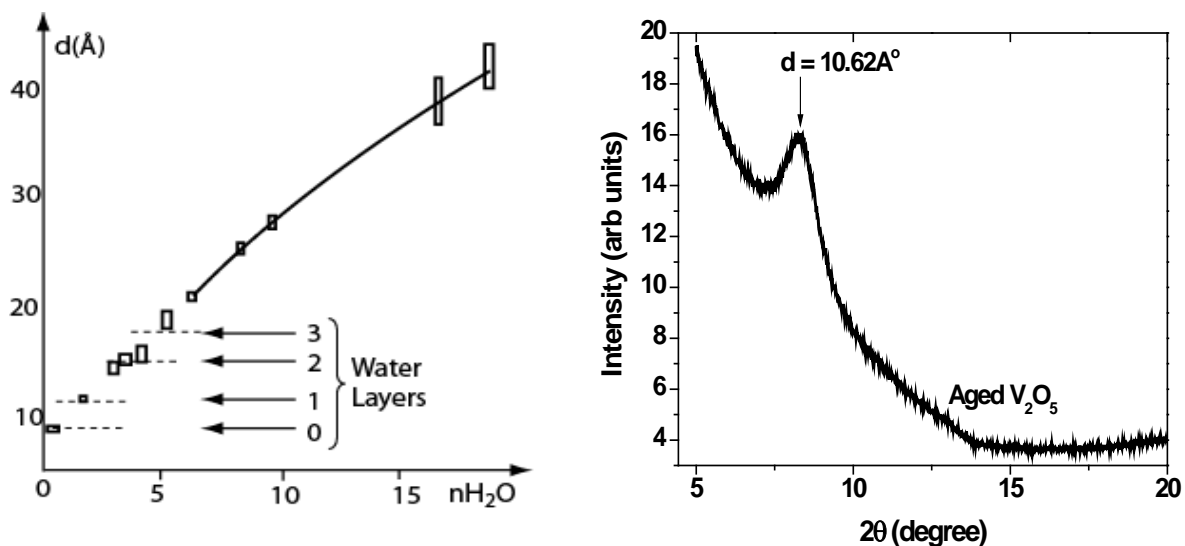


Figure 5. 2. Left, variation of interplanar distance, d in V_2O_5 with intercalated water (adapted from Aldebert et al.^[111]). Right, XRD of individual, aged 90nm thick V_2O_5 film from 2θ $5^\circ \rightarrow 20^\circ$. The peak at $2\theta = 8.2^\circ$ corresponds to an interplanar distance, d of 10.62Å of the basal plane of the orthorhombic phase in V_2O_5

The degree of intercalation as a function of H_2O adsorbed in V_2O_5 gels has been characterized in the past using x-ray diffraction (XRD).^[111] This data is reprinted as reference in **Figure 5. 2, left** and shows the variation of basal plane distance ' d ' of the orthorhombic V_2O_5 phase with the number ' n ' of water molecules associate with a unit molecule of V_2O_5 . For example, V_2O_5 sample with d of $\sim 8.8\text{Å}$ has an ' n ' of 0.5 and higher d indicates intercalated H_2O caused by the 'swelling' of the V_2O_5 network of square pyramidal-like structures.^[112] In **Figure 5. 2, right** we present XRD data generated on aged V_2O_5 films from our own work. A peak at $2\theta = 8.2^\circ$ corresponding to an interplanar distance, d of $\sim 10.62\text{Å}$ is shown. With the help of data extrapolated from **Figure 5. 2 left**, we predict that a $d \sim 10.62\text{Å}$ corresponds to ' n ' of ~ 1.3 in

V₂O₅.nH₂O films. We further note that a fresh V₂O₅ film produces no such peak and is thus indicative of an amorphous film.

Electrical characterization of V₂O₅ and ZnO films

Room temperature Hall measurements were performed on aged V₂O₅.nH₂O and ZnO films. It is to be noted that fresh as well as annealed V₂O₅ films yielded very high resistances (> 10 MΩ) and thus no Hall data could be obtained on these films. Contrary to most prior findings, we report p-type conductivity in our aged V₂O₅.nH₂O films with a net positive concentration of $7.1 \pm 3.6 \times 10^{16} \text{ cm}^{-3}$ and Hall mobility (μ_{HALL}) of $0.22 \pm 0.15 \text{ cm}^2/\text{V-s}$ for a 30nm thick film. The above measurements were performed on multiple samples where the films were aged for at least 48 hours, resulting in Hall coefficients that all yielded stable, positive values indicative of a p-type film. For ZnO films, electron concentrations of 10^{19} cm^{-3} and $\mu_{\text{HALL}} 17.7 \text{ cm}^2/\text{V-s}$ were obtained.^[113]

Next, V₂O₅.nH₂O films were tested for dc conductivity, shown in **Figure 5.3**. The temperature was varied from 250K-340K. Room temperature conductivity (σ_{RT}) of $2 \times 10^{-3} \text{ S/cm}$ was obtained. Using the small polaron hopping model given as^[114]

$$\sigma T = A \exp\left(-\frac{E_a}{kT}\right) \quad (1)$$

where, σ is conductivity, T is temperature and A is a constant, we calculated an activation energy (E_a) of 0.31eV. Both σ_{RT} and E_a are very close to the reported value of 10^{-3} S/cm and 0.35eV by Badot et al.,^[115] for protonic conduction in V₂O₅ gels.

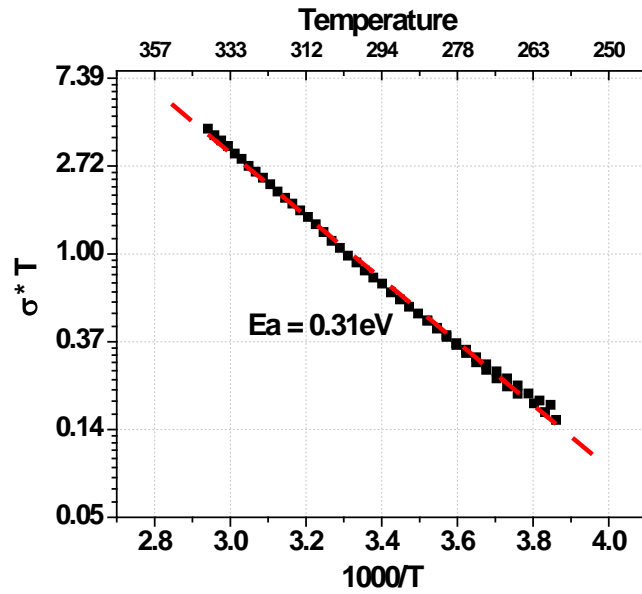


Figure 5. 3. Temperature vs. conductivity data for aged, 30nm V_2O_5 film shows an activation energy (E_a) of 0.31 eV, indicative of H_3O^+ conduction in the films. The dotted (red) line is a fit to the data.

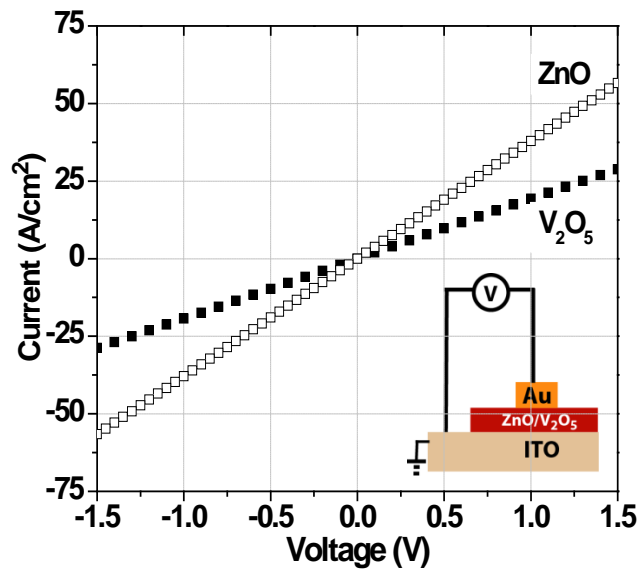


Figure 5. 4. IV curves of ITO- V_2O_5 -Au and ITO-ZnO-Au films showing ohmic behavior

Metal-semiconductor junctions of the individual films were also evaluated to confirm that the metal-semiconductor contacts were Ohmic and not Schottky (rectifying) in character. Current-voltage (IV) curves are shown in **Figure 5. 4** for devices consisting of ITO (bottom electrode, BE)- $V_2O_5.nH_2O$ -Au and ITO (BE)-ZnO-Au. In both instances linear behavior was obtained indicating ohmic contacts. Higher conductance was obtained in ZnO as compared to $V_2O_5.nH_2O$, consistent with higher carrier concentration and mobility in ZnO as obtained from Hall measurements above. Further, BE materials such as Ru and Pt thin films were also tested with $V_2O_5.nH_2O$ and ZnO and Ohmic contacts were verified. The choice of BE materials will be explained below.

Electrical characterization of $V_2O_5 - ZnO$ junctions

Heterojunction devices consisting of three types of bottom electrodes (BE) and $V_2O_5.nH_2O$ -ZnO films were tested for IV characteristics. The BE were 1) conducting ITO on glass substrates 2) ALD Ru electrodes on 100nm of CVD SiO_2 on Si and 3) sputtered Pt electrodes deposited on 100nm of CVD SiO_2 on Si . The rationale for choosing these three electrodes was to modulate the oxygen content at the interface between various BE and $V_2O_5.nH_2O$. Whereas ITO is expected to be a rich source of oxygen, Ru is expected to have relatively small amounts of native RuO_2 on its surface due to ambient oxidation (see Appendix 3 for XPS on Ru) and Pt should have negligible oxide on its surface, leading to little chemical interaction with the overlying $V_2O_5.nH_2O$. **Figure 5. 5 left** and **right** show an IV curve obtained from a Pt(BE)- $V_2O_5.nH_2O$ -ZnO-Au stacked device plotted with linear and log-linear axes,

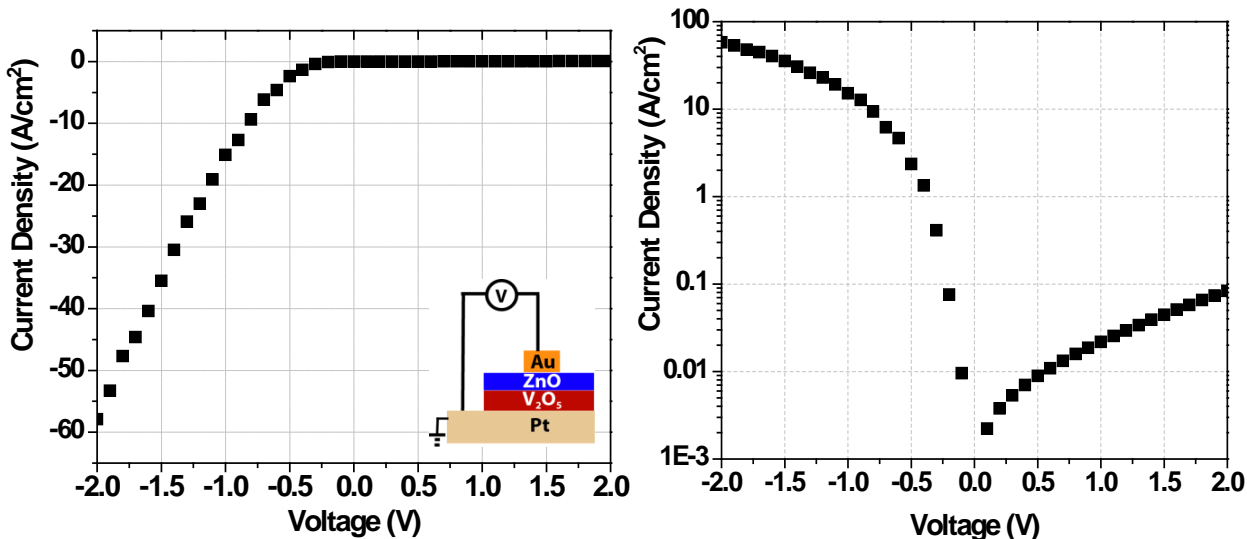


Figure 5.5. Left, IV characteristics of V_2O_5 - ZnO diode with Pt BE. The thickness of the V_2O_5 is ~ 30 nm while ZnO is 100nm. Right, semi-log plot of the graph on left.

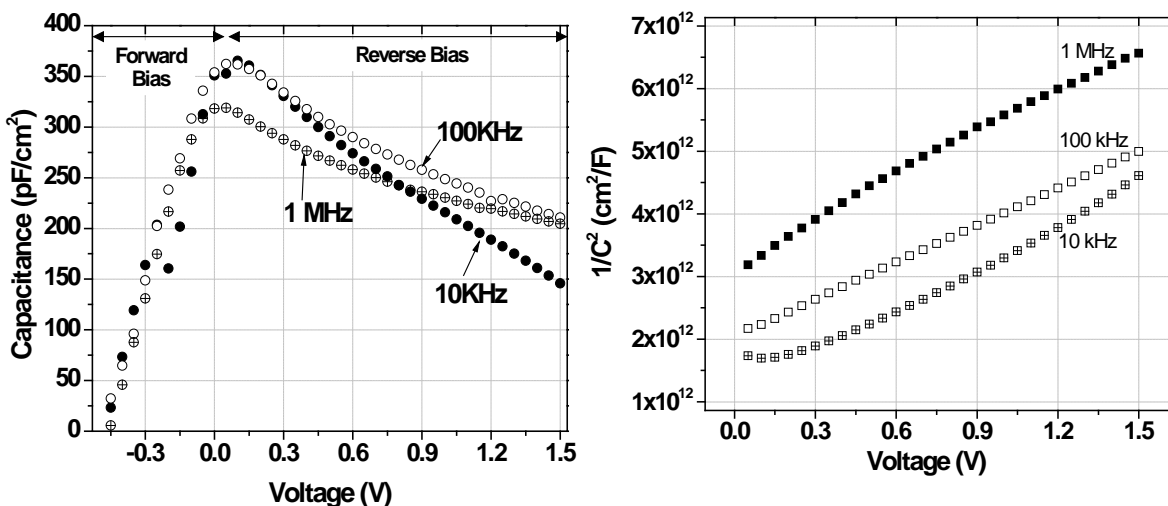


Figure 5.6. Left, capacitance-voltage curves at 3 frequencies. The capacitance decreases with increased reverse bias due to increase in depletion width. Under forward bias, the capacitance drops off rapidly due to non-radiative recombination of minority carriers. Right, $1/(\text{Capacitance})^2$ vs. bias voltage (V) of the diode as function of frequency under reverse bias conditions. The slope of the plot allows one to estimate dopant densities.

respectively. Diode behavior was observed in these devices where a negative voltage on the Au top electrode (ZnO side) forward biased the device while a positive voltage caused reverse biasing. The ratio of the forward bias to reverse bias current, I_{on}/I_{off} is a measure of the rectification observed in diodes. This ratio was obtained at $\pm 2V$ for all our devices. For the device provided in **Figure 5. 5 left and right**, I_{on}/I_{off} is 598. Frequency dependent capacitance voltage (CV) curves were obtained for the diodes. **Figure 5. 6 left** shows CV curves covering a broad frequency range – 10KHz, 100KHz and 1MHz. As the voltage is swept from reverse bias to forward bias (i.e. from positive to negative), the capacitance should monotonically increase signifying a decrease in the depletion width. However, for $V < 0.2V$ a drop in capacitance occurs. Such a capacitance ‘roll-off’ is often seen in organic light emitting diodes (OLEDs) where the roll-off has been attributed to non-radiative processes such as recombination of minority carriers at charged trap centers.^[116] The charge neutralization leads to a drop of capacitance of the structure. Thus, the capacitance roll-off is indicative of a device whose forward bias characteristic is limited by minority carrier recombination.

For the various BE tested, **Table 5. 1** provides a summary of the I_{on}/I_{off} ratios at $\pm 2V$. The best performance characteristics (i.e. I_{on}/I_{off}) are obtained for devices which have Pt electrodes as the BE, where $I_{on}/I_{off} \sim 598$. On the other hand, when ITO, a conducting oxide, is used as a BE, a much smaller $I_{on}/I_{off} \sim 19$ is obtained. Pt is not expected to have an oxygen-rich interfacial layer in contact with the $V_2O_5 \cdot nH_2O$, whereas the oxygen in ITO represents a significant source of oxygen at the interface with $V_2O_5 \cdot nH_2O$. I_{on}/I_{off} for Ru BE lies between Pt and ITO, indicative

Bottom Electrode	V ₂ O ₅ Thickness	ZnO Thickness	I _{on} /I _{off} @ 2V
ITO	30nm	100nm	19
Ru	30nm	100nm	45
Pt	30nm	100nm	598

Table 5. 1. Comparison of I_{on}/I_{off} ratio at ±2V for V₂O₅.nH₂O-ZnO with various bottom electrodes. The Pt BE shows the best performance with the highest I_{on}/I_{off} ratio. The top electrode in all cases was Au.

of moderate amounts of oxygen at the V₂O₅.nH₂O interface as expected from interfacial RuO₂ created by ambient oxidation of the exposed Ru film (see Appendix 3). These results illustrate the deleterious effects of interfacial oxygen for the device characteristics of V₂O₅.nH₂O – ZnO diodes.

Discussion:

It is known from sol-gel synthesis of V₂O₅ films^[117] that using alkoxide based precursors can lead to the reduction of V⁵⁺ → V⁴⁺ due to the presence of C from the alkoxy ligands. Since our ALD chemistry involves an alkoxide based reaction cycle, such a reduction may occur in the V₂O₅ films used in this study. The reduction of the vanadium ion from V⁵⁺ to V⁴⁺ state adds to the electronic conductivity of the film.

In the case of V₂O₅ preparation by ALD, it appears that water-related species have an even larger influence on material properties. Remnant H₂O from the ALD process and/or subsequent adsorption of ambient moisture during aging adds to ionic (protonic) conduction in these films and results in a net positive carrier concentration as borne out by consistent trends between FTIR, XRD, Hall measurements and temperature-based dc conductivity of aged V₂O₅.nH₂O films. When basal plane

distance in $V_2O_5.nH_2O$ films, σ_{RT} of $\sim 2 \times 10^{-3}$ S/cm and resultant $E_a \sim 0.31$ eV of the aged films are considered, we predict using previous literature data,^[111, 115] the water content to be given by $V_2O_5.nH_2O$, where $n \sim 1.3$.

One can extract further information from an analysis of reverse bias capacitance data from **Figure 5. 6 left** by linearizing the capacitance-voltage for pn heterojunctions given as^[10]

$$C = \left[\frac{e \epsilon_0 \epsilon_{ZnO} \epsilon_{V_2O_5} N_{ZnO} N_{V_2O_5}}{2(\epsilon_{ZnO} N_{ZnO} + \epsilon_{V_2O_5} N_{V_2O_5})(V_{bi} - V)} \right]^{1/2} \quad (2)$$

Here, e = elementary charge, ϵ_0 = dielectric permittivity of free space, ϵ_x = dielectric constant of 'x', N_x = carrier density of 'x', x being the film (ZnO or V_2O_5), V_{bi} is the built-in voltage and V , the applied voltage. This allows one to obtain carrier densities of the $V_2O_5.nH_2O$ by measuring the slope of the plot of $1/C^2$ vs. reverse bias voltage. From the slope of the resultant Mott-Schottky plot shown in **Figure 5. 6, right** one can extract $N_{V_2O_5}$ (given^[7], $\epsilon_{ZnO} = 8.6$, $N_{ZnO} = 10^{19}$ cm^{-3} from Hall data above). Unfortunately, reported values of dc dielectric permittivity for $V_2O_5.nH_2O$ vary by two orders of magnitude in the literature (from 100-10000),^[118] suggesting p carrier densities of 5×10^{17} cm^{-3} to 5×10^{15} cm^{-3} for $\epsilon_{V_2O_5} = 10000$ and 100, respectively. The Hall measurements indicate $V_2O_5.nH_2O$ carrier concentrations of $7.1 \pm 3.6 \times 10^{16}$ cm^{-3} which is in the middle of the projected range as calculated above.

Our results are the first Hall report of p-type behavior in ultrathin (~ 30 nm) ALD-based unannealed, $V_2O_5.nH_2O$ films. Previous Hall conductivity measurements of V_2O_5 gels have been carried out but the thickness of the film was large ($10 \mu m$) and the methodology of sample preparation was fast quenching of molten melts.^[119] Badot

et al., have measured electrical properties of ALD V_2O_5 but only after annealing at 500°C for 2 hours, thus rendering the films crystalline.^[120] Both these synthesis approaches produced electronically active, n-type V_2O_5 . Successful Hall measurements on ionic systems however have been done in the past in systems where ionic conduction is highly correlated.^[121] Further study of the structure and chemical composition of as-deposited ALD and annealed films is currently underway, in particular to explore means to tune electronic vs. ionic conductivities *in-situ* during ALD.

In light of the above discussion, the effect of bottom electrode can be explained by the availability of free O atoms from oxygen rich electrodes to annihilate oxygen vacancies and hence oxidize the $V^{4+} \rightarrow V^{5+}$. This should inhibit electronic conductivity in $V_2O_5.nH_2O$ and reduce minority carrier transfer under forward bias i.e., electrons injected from ZnO to $V_2O_5.nH_2O$. Further, V oxidation may disturb the charge balance of the $V_2O_5.nH_2O$, in particular the dipole moment of the vanadyl bond (V=O). It is known that the oxygen associated with this bond is responsible for hydrogen bonding with H_2O . Thus, an increase in the dipole moment of the V=O bond may increase hydrogen bonding and affect proton mobilities within the $V_2O_5.nH_2O$ network.

The unique characteristic of the aged, $V_2O_5.nH_2O$ -ZnO heterojunction diodes is that the rectification observed may be due to conductivity mechanisms strikingly different in the n and p materials. The schematic of the proposed mechanism is shown in **Figure 5.7**. Whereas the p-type region is both proton and electron conducting, the n-type material is electron conducting only. During forward biasing, minority carrier

injection of e^- occurs from ZnO into $V_2O_5 \cdot nH_2O$. The lifetimes of the e^- may be long enough, given that electronic conductivity occurs in $V_2O_5 \cdot nH_2O$ films via electron hopping from a V^{4+} site to V^{5+} (i.e., polaron hopping). At the same time, proton injection from p-type $V_2O_5 \cdot nH_2O$ into ZnO should also occur. It is conceivable that the protons may be trapped at point defects within the ZnO or may recombine resulting in the evolution of H_2 . This further implies that by forward biasing the

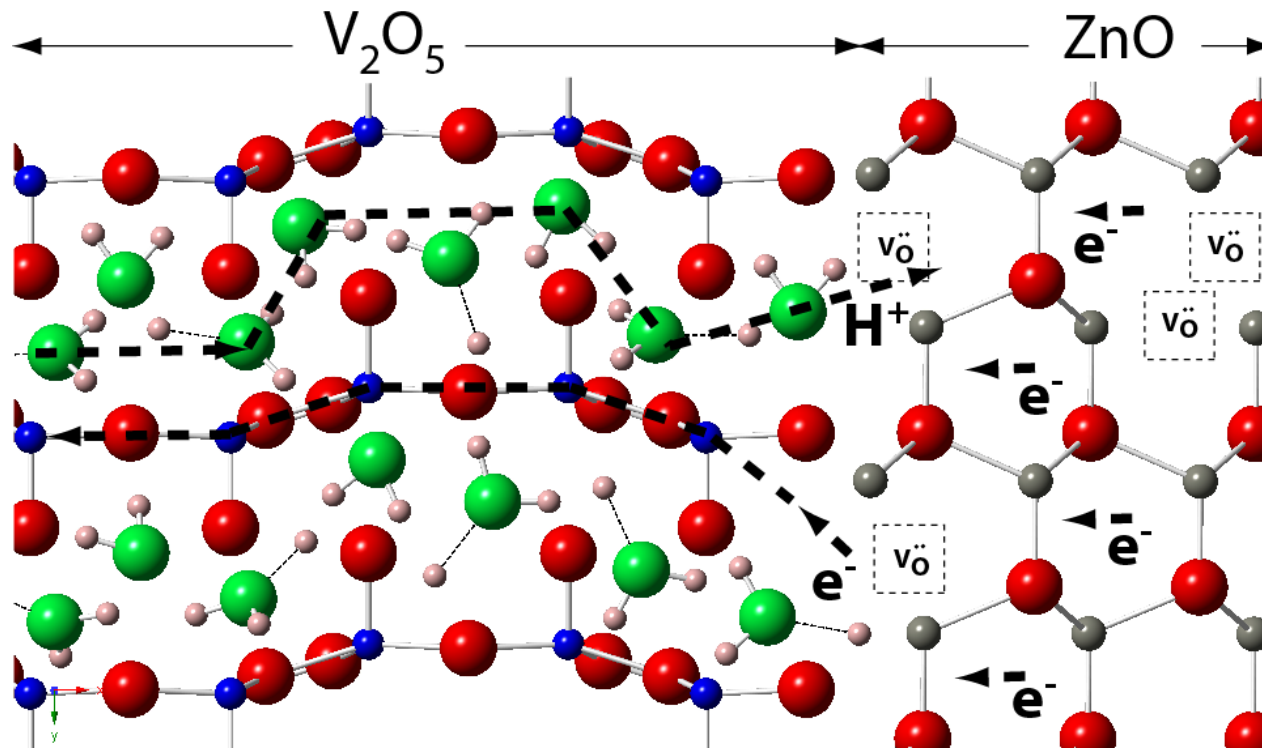


Figure 5. 7. Schematic of the $V_2O_5 - ZnO$ interface showing possible mechanism of charge transport across the $V_2O_5 - ZnO$ interface. The O atom associated with V_2O_5 and ZnO is shown in red. For clarity, the O atom associated with intercalated H_2O and H_3O^+ is shown in green. The blue atoms refer to V, grey atoms belong to Zn and pink atoms are H. The oxygen vacancies (V_o^{**}) in ZnO are labeled as such. During forward bias and within V_2O_5 , protonic conduction occurs via intercalated water and electronic conduction occurs via transfer of charge from $V^{4+} \rightarrow V^{5+}$.

diodes, the water content in the $V_2O_5.nH_2O$ films may become depleted over a period of time. However, in our course of experiments spanning three months, we have not observed the diode characteristics degrade.

Finally, we believe that this work has shown the successful integration of $V_2O_5.nH_2O$ – a mixed ionic-electronic conductor, in a pn junction. Band offsets at the interface of $V_2O_5.nH_2O$ and ZnO which are crucial to determining much of the current-voltage characteristics of heterojunctions have not been addressed in this work but should be carefully evaluated in future studies. The quality of electrode-semiconductor interfaces and pinning of Fermi levels may significantly impact device characteristics as well. Despite these unknowns, good rectification with I_{on}/I_{off} ratios of 598 for the $V_2O_5.nH_2O$ – ZnO system is certainly impressive.

Conclusions:

Aged, $V_2O_5.nH_2O$ -ZnO film stacks were deposited using an all ALD, low temperature ($<150^\circ\text{C}$) deposition scheme. The device structure was shown to be rectifying. The rectification is attributed to the n-type behavior of ZnO and p-type behavior of $V_2O_5.nH_2O$. Whereas n-type behavior in ZnO occurs due to the presence of electrons donated via oxygen vacancies, p-type behavior in $V_2O_5.nH_2O$ is likely a result of intercalated H_2O resulting in proton (H^+ or H_3O^+) conduction. Since, both electronic and ionic conduction are possible in $V_2O_5.nH_2O$, the layer by layer deposition via ALD followed by atmospheric aging seems to create a conducive condition whereby the V_2O_5 can be made proton conducting. Further, the rectification was found to be a strong function of the nature of bottom electrodes. For oxygen rich

electrodes such as ITO, a low I_{on}/I_{off} ratio (19) was observed whereas for noble metal electrodes such as Pt, a high I_{on}/I_{off} ratio (598) was observed. This result points to the deleterious effects of oxygen atoms in oxidizing the V^{4+} states to V^{5+} in the $V_2O_5 \cdot nH_2O$ thereby degrading current voltage characteristics. Further efforts to understand and control conductivity in ALD V_2O_5 films are underway with special emphasis on defining conditions and protocols for aging. The devices described herein can find suitable uses in sensors and transparent and flexible electronics.

Chapter 6: Three-dimensional nanotubular diodes using integrated atomic layer deposition scheme

Abstract:

Simple, scalable strategies for building 3D high aspect-ratio pn junctions are demonstrated. The device consists of n-type Al-doped ZnO and p-type hydrated vanadium oxide fabricated using atomic layer deposition of individual films inside nanoporous anodic aluminum oxide templates. The bottom insulating Al₂O₃ barrier layer is thinned via a controlled voltage ramp-down during anodization and completely removed with a wet isotropic etch. This procedure increases pore diameters, maximizing available volume of active material deposited inside pores while simultaneously exposing the underlying, conducting Al substrate. Templates with pore depths of 0.5, 1 and 2 μm and aspect ratios (pore depth: pore diameter) of 5.5, 11 and 22 respectively, are used to fabricate the nanodiodes. The highest I_{on}/I_{off} ratio ~ 16.7 is obtained for 0.5 μm pore depth sample.

Introduction:

The design, fabrication and control of 3D porous nanostructures to build electronic devices present exciting opportunities in nanotechnology research. An important motivation to work with 3D porous nanostructures is its ability to enhance areal densities and hence improve device characteristics. This is especially true in cases where a device functions via charge transfer or storage across an interface. The approach has been demonstrated to great effect in nanocapacitors,^[3] batteries^[122, 123] and DSSC.^[124]

While many strategies exist to realize 3D porous nanostructures and build functional devices, the combination of self-assembled porous nanotemplates with self-limited, thin film deposition technique offers obvious advantages most notably, conformal deposition of functional films leading to highly reliable devices, significant cost savings due to lithography-free processing and massive scalability. In this paper, we utilize anodic aluminum oxide (AAO) self-assembled, 3D porous nanostructures^[125] in conjunction with atomic layer deposition (ALD), a self-limited deposition technique^[34] to build 3D nanodiodes. The two approaches are highly complementary, the AAO process allowing the formation of lithography-less, highly ordered 3D porous nanostructures^[126] while ALD conformally coating the resulting high aspect ratio, porous templates with high quality thin films of precise thickness.^[46] Our material set consists of n-type Al-doped ZnO and p-type $V_2O_5 \cdot nH_2O$ (i.e., hydrated vanadium oxide) – a system that has shown strong rectification as planar diodes via a mixed electronic-ionic conduction mechanism.^[127] This paper demonstrates simple and highly controllable strategies for developing 3D nanotubular diodes using AAO templates in conjunction with ALD.

Experimental Details:

AAO templates were prepared on high purity Al foils using a 2-step anodization technique^[24] in 0.3M oxalic acid bath maintained at 8°C. A circular aperture, 1cm wide of Al foil was exposed to the anodization solution. Within this region, pore densities of 10^{10} cm^{-2} were obtained. As grown pore diameters of 35nm and interpore distances of 110nm were measured. A pore growth rate was obtained $\sim 72\text{nm/min}$, thus allowing the time of the second anodization step to control pore depth of the

templates. Prior to the end of the second anodization process, a controlled voltage ramp-down was applied to the template. This initiated branching at the pore tip (**Figure 6. 1a**). A subsequent wet etch step in 5wt% H_3PO_4 allowed the pores to a) widen pore diameters to 90nm and b) remove the insulating Al_2O_3 barrier layer (BL) completely, thus exposing the conducting Al substrate underneath (**Figure 6. 1b**). These set of samples were labeled 'BL open'. Another set of samples were pore widened only to 80nm without the voltage ramp-down procedure and therefore without exposing the Al substrate. In this case, 20nm of BL remained at the bottom of the pore and the samples were labeled 'BL closed'.

A BENEQTM TFS 500 reactor was used for ALD deposition. First, 21nm of conducting, 3at% Al-doped ZnO (AZO) was deposited inside the templates. The AZO layer was expected to act both as an electrode and as an n-type layer. Next, 24nm V_2O_5 was deposited inside the pores without breaking vacuum. This is shown in **Figure 6. 1c**. The total thickness of the material deposited inside a pore is then given as $2(t_{\text{ZnO}} + t_{\text{V}_2\text{O}_5}) = 90\text{nm}$, where t_{ZnO} and $t_{\text{V}_2\text{O}_5}$ are thicknesses of ZnO and V_2O_5 , respectively. Thus, the ALD deposition was expected to fully fill a 90nm wide pore. However, as shown in high resolution SEM images in **Figure 6. 1d**, a thin volume along the length of the pore could not be filled. Process details about both ALD ZnO^[11] and ALD V_2O_5 are provided elsewhere. It is to be noted however, that H_2O was used as the oxidant in both the films. Finally, 250 μm wide Au electrodes were sputtered using a shadow mask in a Denton Desktop III system.

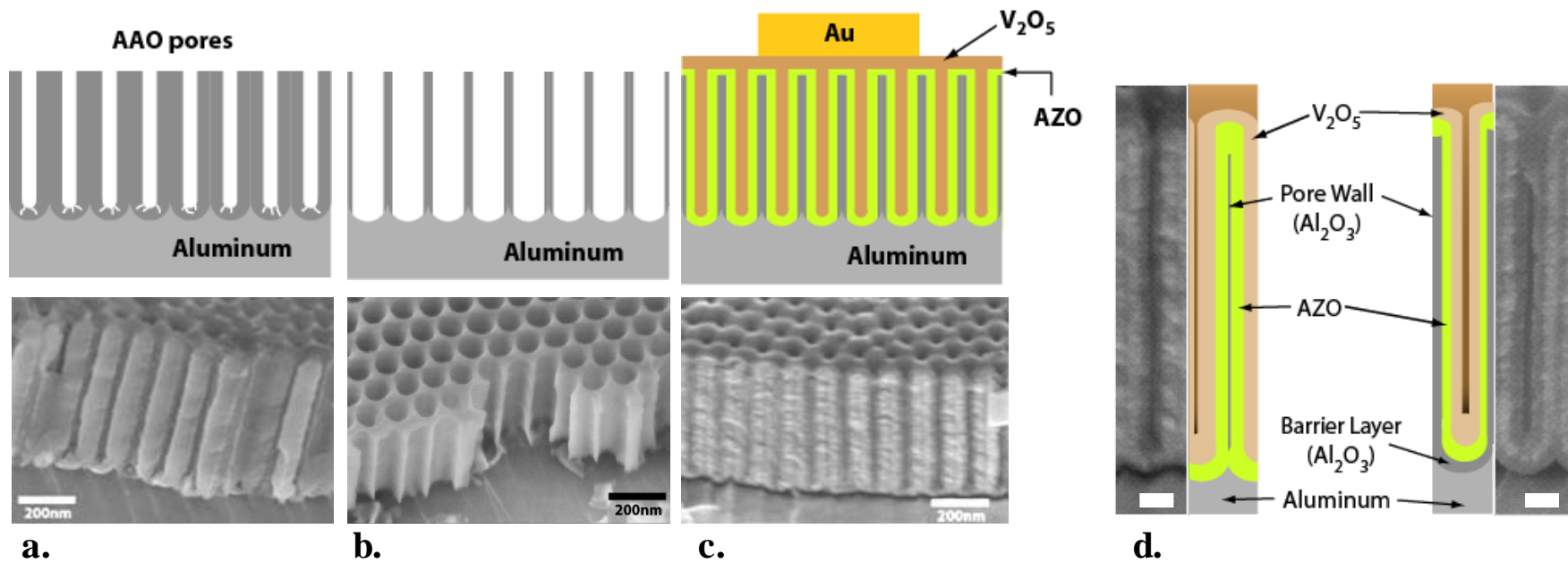


Figure 6. 1 : a-c: Schematic (top row) for preparing 3D nanodiodes with 'BL open' scheme and corresponding SEM images (bottom row) a) AAO template formation with branching at bottom b) Pore widening and barrier layer opening c) ALD of AZO and V₂O₅ films followed by Au sputter through shadow mask. The Al foil served as the back contact whereas the Au was used as the top contact d) Comparison of 'BL open' (left) and 'BL close' (right) samples. The scale at the bottom of the SEM images in 'd' represents 50nm.

Results and Discussion:

The nanostructural difference between ‘BL open’ and ‘BL close’ samples are shown in **Figure 6. 1d** both schematically as well as with SEM images. By virtue of the processing scheme described above for sample set ‘BL open’, the AZO film was shunted with the Al at the bottom of every nanopore. However for sample set ‘BL close’, the AZO film was insulated from the Al at the bottom of the pore. For these set of samples, electrical contact could only be established outside the region of pore growth which was 1cm wide.

The difference in electrical properties of nanotubular diodes with and without the insulating BL is shown in **Figure 6. 2**~~Error! Reference source not found.~~ where diode IVs are plotted in a semi-log plot for clear comparison between the two curves. Rectification is achieved with I_{on}/I_{off} of 16.7 and 14.4 for the ‘BL open’ and ‘BL

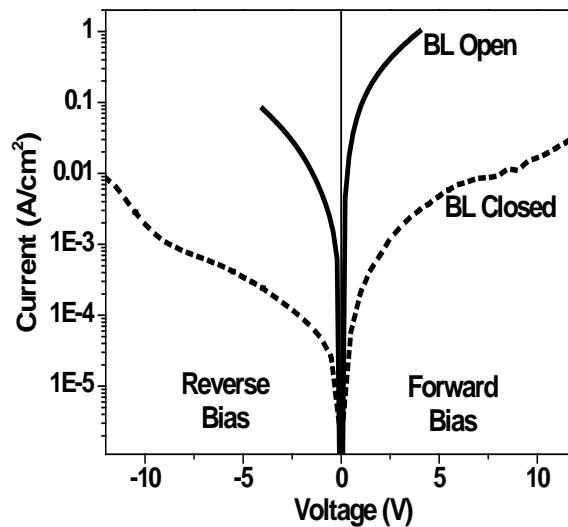


Figure 6. 2. Diode IV characteristics on a semi log scale for the BL open and BL close samples. Current density is calculated based on total area exposed, accounting for the enhancement due to the porous nanostructure.

close' samples respectively. However, the current in 'BL open' is more than 2 orders of magnitude higher than sample 'BL close'. Whereas for the former case, current collection is efficiently achieved at the bottom of individual nanodiodes, current has to travel across the aperture region of pore growth in the 'BL close' samples, thus adding to higher series resistance of the devices.

Individual IV curve on a linear scale is shown in **Figure 6. 3, left** for the 'BL open' sample. The turn-on voltage (V_o) can be extracted from the IV curves by linearly extrapolating the forward bias current to zero. V_o is found to be 1.25V for 'BL open' sample and 7.5V for the 'BL close' sample (not shown). Clearly, providing good contact to every nanotubular diode through the Al substrate helps in reducing the series resistance of the device and voltage regime for device operation.

Figure 6. 3, right shows the effect of AAO pore depth on the I_{on}/I_{off} characteristics of the diodes. It can be seen that introducing 3D nanoarchitecture into the processing scheme leads to decrease in the I_{on}/I_{off} ratio and hence results in degradation of the devices.

To understand this trend, we briefly explain the nature of the AZO- $V_2O_5.nH_2O$ diodes.^[127] Whereas, the AZO film is electronically conducting – rendering it n-type, our processing using ALD allows V_2O_5 films to be hydrated and become proton (H^+) conducting, thus making the films p-type. The rectification in these devices result from the mixed electronic-protonic conductivity of the AZO and V_2O_5 films, respectively. Thus, the presence of H^+ is a necessary requirement in V_2O_5 films as the hydration of the V_2O_5 films is key to preparing p-type V_2O_5 films.

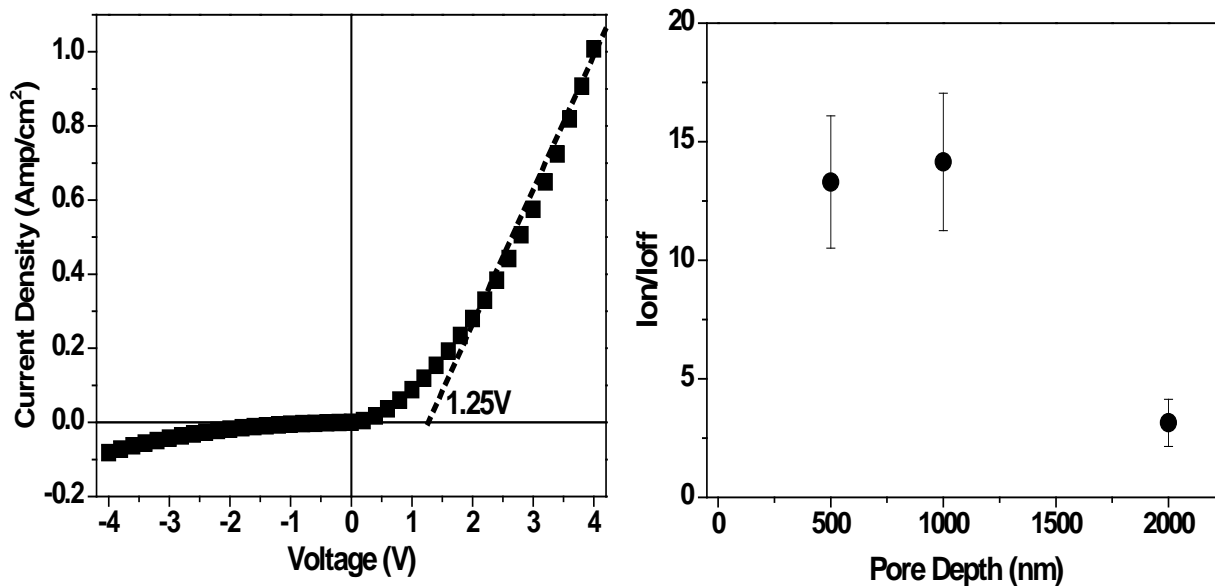


Figure 6. 3. Left, IV characteristics of BL open sample showing the rectification behavior. The extrapolation of the forward bias region to current density = 0, provides the turn-on voltage $V_0= 1.25V$. Right, variation of I_{on}/I_{off} as a function of the pore depth in nanotubular diodes.

We know that while the bottom surface of V_2O_5 is intimately in contact with AZO, the top surface of the V_2O_5 is contacted to Au electrodes at the pore openings only. Thus during forward bias, e^- injected into the V_2O_5 film have to travel the length of the pore before being collected at the Au electrode at the top. This adds to the series resistance of the structure and therefore deeper the pore, higher this resistance. While the effect of increased series resistance can be minimal on the reverse bias leakage current (the reverse bias resistance of diodes already being high), forward bias characteristics can be significantly degraded and can thus lead to a lowering of the I_{on}/I_{off} ratios as observed in **Figure 6. 3 right**. Strategies to counter these effects

could include using an ALD-based noble metal as a top electrode to conformally coat the V_2O_5 top surface.

Conclusions:

In conclusion, we have demonstrated rectifying, 3D nanotubular diodes comprising of AZO as an n-type layer with hydrated $V_2O_5 \cdot nH_2O$ as a p-type layer. This device is built inside 3D, self assembled AAO nanoporous templates. By using a controlled ramp-down technique during anodization process we are able to selectively remove the insulating BL from the bottom of a nanopore and use this scheme to shunt the conducting Al substrate to the device at the bottom of each individual nanopore. This leads to a large drop in series resistance, increase in the forward bias current and a reduction in turn-on voltage from 7.5V to 1.25V. Our results also suggest that increasing pore depth may adversely affect I_{on}/I_{off} ratio of the diodes, possibly a result of increased series resistance of the films involved. I_{on}/I_{off} ratio as high as 16.7 is obtained in the diodes.

Chapter 7: Conclusions and scope for future work

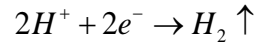
In this thesis, three main objectives have been achieved –

1. The use of ALD's self-limited reaction sequence for building nanolaminate thin films of Al-doped ZnO - It was shown that at% Al doping could easily be varied by maintaining a simple ratio of the cycles of ZnO to Al₂O₃. All the structural, electrical and optical properties were closely correlated to one another. The work highlighted the ease of fabrication and strict control over nanoalloy composition that could be achieved via ALD.
2. By using integrated ALD sequences of two different materials with vastly different properties, novel devices could be fabricated - In this case, it was shown that electronically conducting, n-type ZnO and ionically conducting, p-type V₂O₅.nH₂O films could be placed in a layered structure to form pn junction diodes using an all ALD sequence at a low temperature of 150°C. The new device, termed as a 'mixed ionic-electronic device' was found to have rectification given by I_{on}/I_{off} as high as 598.
3. Finally, using the sequence of films demonstrated in '2' above, within a nanoporous AAO template, once could build 3D nanotubular pn junctions. Diodes with rectification as high as 16.7 was obtained in nanopores which were only 90nm wide and up to 1µm deep.

While the demonstration of ALD process development for thin films and all-ALD process integration schemes for novel electronic devices is exciting, the work leads one to ask important questions and these can be a source for future work. Namely,

1. What is the nature of recovery of growth in nanoalloyed and nanolaminated films during ALD of multicomponent films? We have shown that a phenomenological model can well explain the recovery of growth rates in Al-doped ZnO films. To a first order, our experiments indicate that an ALD surface reaction may proceed towards completion via surface saturation of reactive sites. However, the next cycle of incoming species, if significantly different in its nature than the parent film, is able to ‘interact’ with chemical species present in the sub-surface (up to ~6 MLs below the surface) as well. Ab-initio or DFT calculations may certainly be helpful to explain why this occurs. Furthermore, one can explore the role and nature of oxidant used. Since H₂O was used as an oxidant for both ALD Al₂O₃ and ZnO, it would be interesting to see the results of recovery and film properties; if for example, O₃ was used as an oxidant source.
2. How can V₂O₅.nH₂O films be prepared insitu during the ALD process? As was shown in chapter 5, the aging process lends the V₂O₅ its p-type character. This occurs as a result of water adsorption followed by intercalation in the V₂O₅. Since H₂O is the oxidant used in the ALD process, it would be beneficial to perform the p-type ‘doping’ during the growth of the V₂O₅ film. This requires a careful investigation of the temperature and the pulse-purge times for the H₂O cycles during the V₂O₅ process.
3. Applied research in mixed ionic-electronic devices: The combination of using electrons and protons for charge transport in a device raises interesting ideas on applied research for such devices. An exciting avenue for research could be

the production of H₂ as a result of the forward biasing of such pn diodes. A possible reaction could be :



where the H⁺ are supplied from the V₂O₅ side and the e⁻ are supplied from the ZnO side. The electrode side of the V₂O₅ film could be in direct contact with a source of water, thus supplying a steady source of H⁺ for the reaction to be sustained for long periods of time. Diffusion of H or H₂ in ZnO is certainly a topic that needs to be addressed separately.

Thus, the avenues for future work represent interesting opportunities that can result in advances in basic scientific studies or technological breakthroughs. The work enclosed in this thesis lays the foundation for such work to be carried out in the near future.

Appendix 1

Example of Process Recipe in BENEQ TFS 500

*Recipe AlZnO_1to20x100_150C

*Recipe for 2.5% Al-ZnO

*Precursors DEZ TMA and Water by own vapor pressures

*Based on flow chart N500112

*TMA at liquid source 4, DEZ in source 3

*Water at liquid source 1

*Source needle valves (NV-PL1 open 1/2 turn, NV-PL3 open 3 turn, NV-PL4 open 25+12.5 division turns)

*Inert gas drain valves (NV-IA open 1.5 turn, NV-IB open 1/2 turn)

*Chiller temperature 20C

*Water pulse without DV-PA , only by own vapour pressure

*Program start

SPROG

*Open the N2 main valve

OPEN DV-N01

*Set flows

FLOW MFC-AS=100

FLOW MFC-BS=100

FLOW MFC-VS=100

*Close pulse valves

CLOSE DV-PL1,DV-BL1,DV-PL2,DV-BL2

CLOSE DV-PL3,DV-BL3,DV-PL4,DV-BL4

CLOSE DV-PG1,DV-PG2,DV-PA,DV-PB

*Close hot source valves

CLOSE DV-BHA1,DV-BHA2,DV-PH1,DV-PH2

CLOSE DV-BH1,DV-BH2

*Check the vacuum level

WUNTIL PIA-P1<10 2s

*Set temperatures

TEMP TIAC-R1S=150

*wait until temperature is ok

WUNTIL TIAC-R1>=TIAC-R1S 5h

*Are temperatures ok to start the process ?

WRITE M5

WUSER YES

WTIME 2s

*open precursor hand valves

WRITE M6

WUSER YES

*Pulsing

REPEAT 100

* 20 ZnO monolayer

REPEAT 20

*DEZ Half Cycle

OPEN DV-PA,DV-PB

WTIME 250ms

PULSE DV-PL3 250ms

WTIME 250ms

Purge 500ms

* Water Half Cycle

OPEN DV-PA,DV-PB

WTIME 250ms

PULSE DV-PL1 250ms

WTIME 250ms

Purge 500ms

REND

* 1 Al₂O₃ monolayer

*TMA Half Cycle

OPEN DV-PA,DV-PB

WTIME 250ms

PULSE DV-PL4 250ms

WTIME 250ms

Purge 500ms

* Water Half Cycle

OPEN DV-PA,DV-PB

WTIME 250ms

PULSE DV-PL1 500ms

WTIME 250ms

Purge 1s

REND

*Close pulse valves

CLOSE DV-PA,DV-PB

CLOSE DV-PL1,DV-BL1,DV-PL2,DV-BL2

CLOSE DV-PL3,DV-BL3,DV-PL4,DV-BL4

CLOSE DV-PG1,DV-PG2,DV-PA,DV-PB

*Close hot source valves

CLOSE DV-BHA1,DV-BHA2,DV-PH1,DV-PH2

CLOSE DV-BH1,DV-BH2

*Use gas ballast 1 min

PULSE DV-NP1 1min

WTIME 2s

*Set temperatures higher than process temp to compensate for opening the chamber

TEMP TIAC-R1S=160

*close precursor hand valves

WRITE M7

WUSER YES

WTIME 2s

*confirm that all precursor hand valves are closed

WRITE M22

WUSER YES

WTIME 2S

*Start TMA and DEZ line purge

WRITE M25

WUSER YES

*Remove residual TMA and DEZ from delivery lines

PULSE DV-PL4 2min

PURGE 1min

PULSE DV-PL3 2min

*end program

EPROG

*-----

Appendix 2

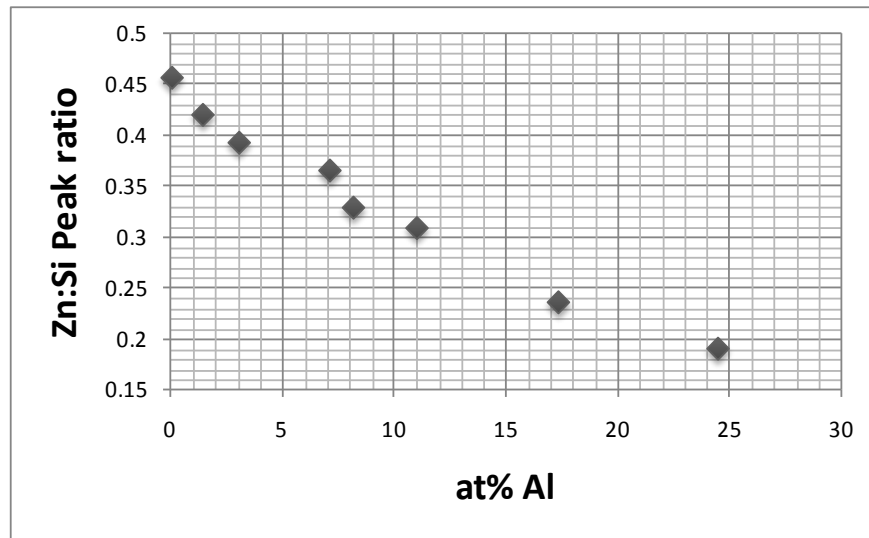
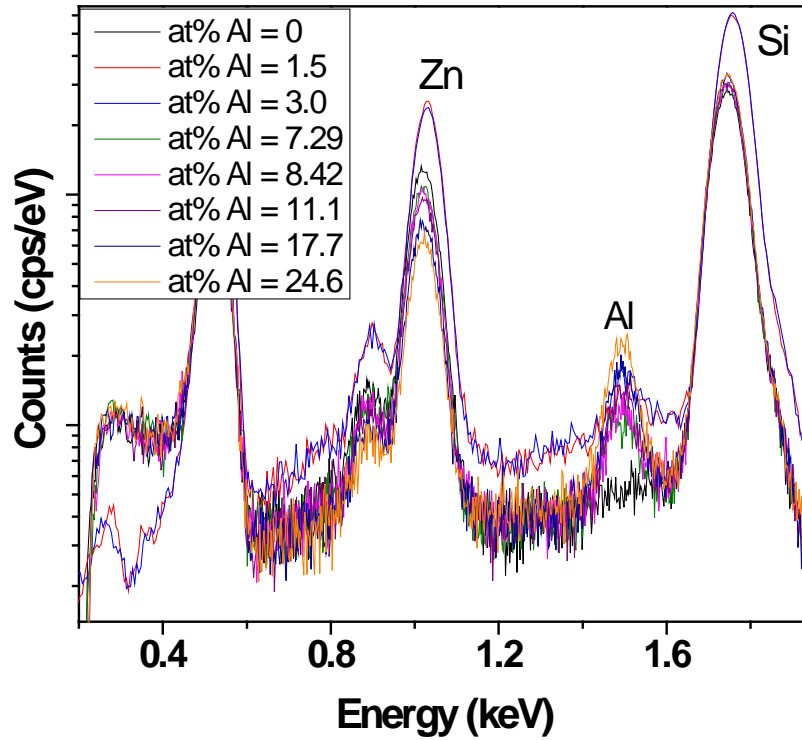
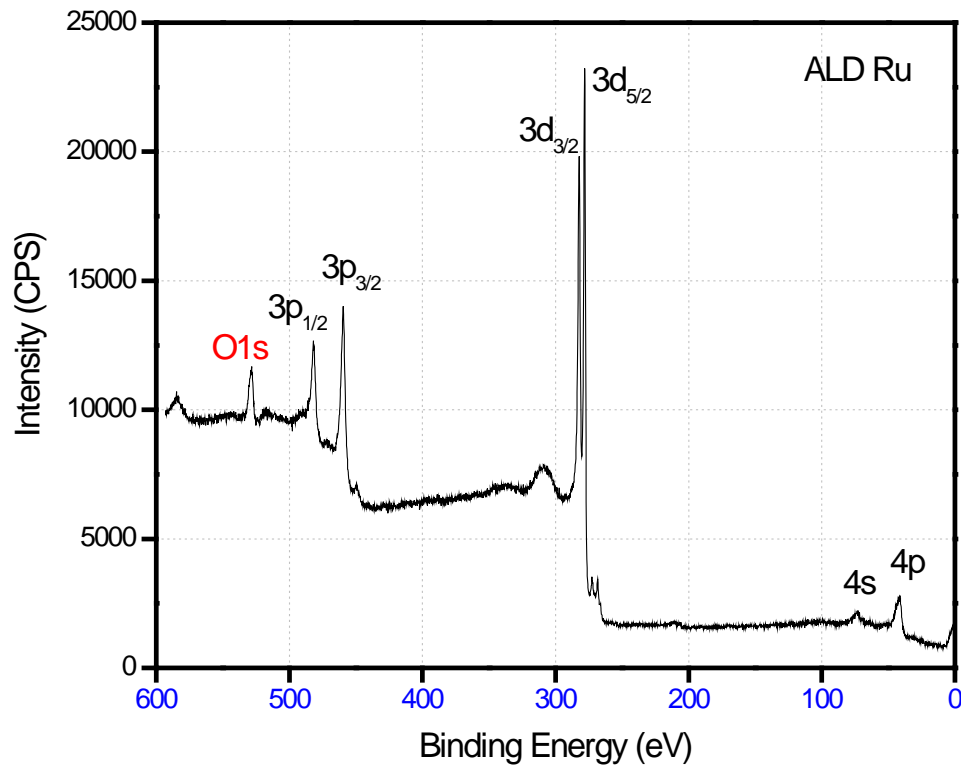


Figure S1: a) EDX profiles for all the AZO samples deposited on high purity quartz substrates. B) The ratio of Zn:Si is plotted against the at% Al. This ratio was used to normalize XRD peak areas.

Appendix 3

Supplementary Figure S 1: X-ray Photoelectron Spectroscopy (XPS) on pure Ru films deposited by ALD. The escape depth of the photoelectrons is around 1nm. The spectrum shows clear peaks of Ru and that of O (marked in red). The Ru 3d 5/2 overlaps with the C 1s making adventitious C determination difficult. Assuming a typical surface C of 10 at% we get a Ru:O of 1.00:0.42 indicating a sub oxide-like RuO_x phase.



Bibliography

- _[1] , D. J. Thurmer, D. Grimm, M. Bauer, O. G. Schmidt, *Nano Letters* **2010**, *10*, 2506.
- _[2]L. F. Zhang, A. Eisenberg, *Science* **1995**, *268*, 1728.
- _[3]P. Banerjee, I. Perez, L. Henn-Lecordier, S. B. Lee, G. W. Rubloff, *Nature Nanotechnology* **2009**, *4*, 4.
- _[4]P. Banerjee, I. Perez, L. Henn-Lecordier, S. B. Lee, G. W. Rubloff, "ALD based metal-insulator-metal (MIM) nanocapacitor for energy storage", presented at *ECS Transactions - Atomic Layer Deposition Applications 5*, **2009**.
- _[5]D. G. Thomas, *Ieee Transactions on Electron Devices* **1971**, *ED18*, 621.
- _[6]H. Y. Fan, *Phys. Rev.* **1949**, *75*, 1631.
- _[7]U. Ozgur, Y. I. Alivov, C. Liu, A. Teke, M. A. Reshchikov, S. Dogan, V. Avrutin, S. J. Cho, H. Morkoc, *J. Appl. Phys.* **2005**, *98*.
- _[8]J. H. Burroughes, D. D. C. Bradley, A. R. Brown, R. N. Marks, K. Mackay, R. H. Friend, P. L. Burns, A. B. Holmes, *Nature* **1990**, *347*, 539.
- _[9]A. W. Ghosh, P. Damle, S. Datta, A. Nitzan, *MRS Bulletin* **2004**, *29*, 391.
- _[10]S. M. Sze, *Physics of Semiconductor Devices*, Wiley-Interscience, **1981**.
- _[11]P. Banerjee, W. J. Lee, K. R. Bae, S. B. Lee, G. W. Rubloff, *Journal of Applied Physics* **2010**, *108*, 7.
- _[12]A. Aguilera, V. Jayaraman, S. Sanagapalli, R. S. Singh, V. Jayaraman, K. Sampson, V. P. Singh, *Sol. Energy Mater. Sol. Cells* **2006**, *90*, 713.
- _[13]G. Patermarakis, C. Pavlidou, *Journal of Catalysis* **1994**, *147*, 140.
- _[14]B. He, Son, S.J., Lee, S.B., *Langmuir* **2006**, *22*, 8263

- _[15]R. Liu, S. Il Cho, S. B. Lee, *Nanotechnology* **2008**, *19*.
- _[16]R. Liu, S. B. Lee, *J Am Chem Soc* **2008**, *130*, 2942.
- _[17]Q. L. Chen, K. H. Xue, W. Shen, F. F. Tao, S. Y. Yin, W. Xu, *Electrochim Acta* **2004**, *49*, 4157.
- _[18]N. Haberkorn, J. S. Gutmann, P. Theato, *Acs Nano* **2009**, *3*, 1415.
- _[19]G. Patermarakis, N. Nicolopoulos, *Journal of Catalysis* **1999**, *187*, 311.
- _[20]A. Eftekhari, Ed. *Nanostructured Materials in Electrochemistry*, Wiley-VCH Verlag GmbH & Co., **2008**.
- _[21]J. P. O' Sullivan, G. C. Wood, *Proc R Soc Lon Ser-A* **1970**, *317*, 511.
- _[22]W. Lee, Ji, R., Gosele, U., Nielsch, K, *Nature Materials* **2006**, *5*, 741.
- _[23]S. Z. Chu, K. Wada, S. Inoue, M. Isogai, Y. Katsuta, A. Yasumori, *Journal of the Electrochemical Society* **2006**, *153*, B384.
- _[24]H. Masuda, K. Fukuda, *Science* **1995**, *268*, 1466.
- _[25]V. V. Konovalov, G. Zangari, R. M. Metzger, *Chemistry of Materials* **1999**, *11*, 1949.
- _[26]J. S. Suh, J. S. Lee, *Applied Physics Letters* **1999**, *75*, 2047.
- _[27]Y. C. Sui, J. M. Saniger, *Materials Letters* **2001**, *48*, 127.
- _[28]T. Ono, C. Konoma, H. Miyashita, Y. Kanamori, M. Esashi, *Japanese Journal of Applied Physics Part 1-Regular Papers Short Notes & Review Papers* **2003**, *42*, 3867.
- _[29]Z. Wu, Richter, C., Menon, L., *Journal of the Electrochemical Society* **2007**, *154*, E8.

- _[30]H. Pan, J. Lin, Y. Feng, H. Gao, *IEEE Transactions on Nanotechnology* **2004**, *3*, 5.
- _[31]Z. Chen, H. G. Zhang, *Journal of the Electrochemical Society* **2005**, *152*, D227.
- _[32]O. Jessensky, F. Muller, U. Gosele, *Applied Physics Letters* **1998**, *72*, 1173.
- _[33]K. Nielsch, Choi, J., Schwirn, K., Wehrspohn, R.B., Gosele, U., *Nano Lett.* **2002**, *2*, 677.
- _[34]S. M. George, *Chem. Rev.* **2010**, *110*, 111.
- _[35]S. M. George, B. Yoon, A. A. Dameron, *Accounts of Chemical Research* **2009**, *42*, 498.
- _[36]H. Kim, H. B. R. Lee, W. J. Maeng, *Thin Solid Films* **2009**, *517*, 2563.
- _[37]M. Leskela, M. Ritala, *Angewandte Chemie-International Edition* **2003**, *42*, 5548.
- _[38]R. L. Puurunen, *Journal of Applied Physics* **2005**, *97*.
- _[39]A. W. O. S. M. George, and J. W. Klaus, *J. Phys. Chem.* **1996**, *100*, 13121.
- _[40]S. M. George, A. W. Ott, J. W. Klaus, *J. Phys. Chem.* **1996**, *100*, 13121.
- _[41]D. J. Lee, H. M. Kim, J. Y. Kwon, H. Choi, S. H. Kim, K. B. Kim, *Adv. Funct. Mater.* **2011**, *21*, 448.
- _[42]Z. A. Sechrist, F. H. Fabreguette, O. Heintz, T. M. Phung, D. C. Johnson, S. M. George, *Chemistry of Materials* **2005**, *17*, 3475.
- _[43]A. Furuya, E. Soda, M. Shimada, S. Ogawa, *Japanese Journal of Applied Physics Part 1-Regular Papers Brief Communications & Review Papers* **2005**, *44*, 7430.

- _[44]J. Biener, T. F. Baumann, Y. M. Wang, E. J. Nelson, S. O. Kucheyev, A. V. Hamza, M. Kemell, M. Ritala, M. Leskela, *Nanotechnology* **2007**, *18*.
- _[45]J. W. Elam, J. A. Libera, M. J. Pellin, A. V. Zinovev, J. P. Greene, J. A. Nolen, *Applied Physics Letters* **2006**, *89*.
- _[46]J. W. Elam, D. Routkevitch, P. P. Mardilovich, S. M. George, *Chemistry of Materials* **2003**, *15*, 3507.
- _[47]I. Perez, E. Robertson, P. Banerjee, L. Henn-Lecordier, S. J. Son, S. B. Lee, G. W. Rubloff, *Small* **2008**, *4*, 1223.
- _[48]J. S. King, D. Heineman, E. Graugnard, C. J. Summers, *Applied Surface Science* **2005**, *244*, 511.
- _[49]M. Leskela, M. Kemell, K. Kukli, V. Pore, E. Santala, M. Ritala, J. Lu, *Materials Science & Engineering C-Biomimetic and Supramolecular Systems* **2007**, *27*, 1504.
- _[50]M. Knez, K. Niesch, L. Niinisto, *Advanced Materials* **2007**, *19*, 3425.
- _[51]R. G. Gordon, D. Hausmann, E. Kim, J. Shepard, *Chemical Vapor Deposition* **2003**, *9*, 73.
- _[52]Y. B. Jiang, N. G. Liu, H. Gerung, J. L. Cecchi, C. J. Brinker, *Journal of the American Chemical Society* **2006**, *128*, 11018.
- _[53]X. H. Liang, S. M. George, A. W. Weimer, *Chemistry of Materials* **2007**, *19*, 5388.
- _[54]L. K. Tan, M. A. S. Chong, H. Gao, *Journal of Physical Chemistry C* **2008**, *112*, 69.

- _[55]C. Jagadish, S. Pearton, Eds., *Zinc Oxide Bulk, Thin Films and Nanostructures*, Elsevier, **2006**.
- _[56]J. N. Duenow, T. A. Gessert, D. M. Wood, T. M. Barnes, M. Young, B. To, T. J. Coutts, *J. Vac. Sci. Technol., A* **2007**, *25*, 955.
- _[57]T. Minami, H. Nanto, S. Takata, *Jpn. J. Appl. Phys., Part 2* **1984**, *23*, L280.
- _[58]F. K. Shan, G. X. Liu, W. J. Lee, B. C. Shin, *J. Appl. Phys.* **2007**, *101*.
- _[59]K. Ellmer, A. Klein, B. Rech, Eds., *Transparent Conductive Zinc Oxide*, Vol. 104, Springer, **2008**.
- _[60]W. S. Lau, S. J. Fonash, *J. Electron. Mater.* **1987**, *16*, 141.
- _[61]S. M. George, A. W. Ott, J. W. Klaus, *J. Phys. Chem.* **1996**, *100*, 13121.
- _[62]J. W. Elam, S. M. George, *Chem. Mater.* **2003**, *15*, 1020.
- _[63]J. W. Elam, D. Routkevitch, S. M. George, *J. Electrochem. Soc.* **2003**, *150*, G339.
- _[64]J. W. Elam, Z. A. Sechrist, S. M. George, *Thin Solid Films* **2002**, *414*, 43.
- _[65]E. Guziewicz, I. A. Kowalik, M. Godlewski, K. Kopalko, V. Osinniy, A. Wojcik, S. Yatsunenko, E. Lusakowska, W. Paszkowicz, M. Guziewicz, *J. Appl. Phys.* **2008**, *103*.
- _[66]P. C. Rowlette, C. G. Allen, O. B. Bromley, A. E. Dubetz, C. A. Wolden, *Chem. Vap. Deposition* **2009**, *15*, 15.
- _[67]Q. H. Li, D. L. Zhu, W. J. Liu, Y. Liu, X. C. Ma, *Appl. Surf. Sci.* **2008**, *254*, 2922.
- _[68]J. Mass, P. Bhattacharya, R. S. Katiyar, *Mater. Sci. Eng., B* **2003**, *103*, 9.

- _[69]J. G. Lu, S. Fujita, T. Kawaharamura, H. Nishinaka, Y. Kamada, T. Ohshima, Z. Ye, Y. J. Zeng, Y. Z. Zhang, L. P. Zhu, H. P. He, B. H. Zhao, *J. Appl. Phys.* **2007**, *101*.
- _[70]S. Y. Pung, K. L. Choy, X. Hou, C. X. Shan, *Nanotechnology* **2008**, *19*.
- _[71]E. B. Yousfi, J. Fouache, D. Lincot, *Appl. Surf. Sci.* **2000**, *153*, 223.
- _[72]D. Lide, *CRC Handbook of Chemistry and Physics, 88th Edition (CRC Handbook of Chemistry and Physics)*, CRC, **2007**.
- _[73]S. Yoshioka, F. Oba, R. Huang, I. Tanaka, T. Mizoguchi, T. Yamamoto, *J. Appl. Phys.* **2008**, *103*.
- _[74]M. H. Yoon, S. H. Lee, H. L. Park, H. K. Kim, M. S. Jang, *J. Mater. Sci. Lett.* **2002**, *21*, 1703.
- _[75]J. Hupkes, B. Rech, S. Calnan, O. Kluth, U. Zastrow, H. Siekmann, M. Wuttig, *Thin Solid Films* **2006**, *502*, 286.
- _[76]R. E. Hummel, *Electronic Properties of Materials*, Springer-Verlag, **1993**.
- _[77]J. G. Lu, Z. Z. Ye, Y. J. Zeng, L. P. Zhu, L. Wang, J. Yuan, B. H. Zhao, Q. L. Liang, *J. Appl. Phys.* **2006**, *100*.
- _[78]G. D. Wilk, R. M. Wallace, J. M. Anthony, *J Appl Phys* **2001**, *89*, 5243.
- _[79]E. Burstein, *Phys. Rev.* **1954**, *93*, 632.
- _[80]T. S. Moss, *Proceedings of the Physical Society of London Section B* **1954**, *67*, 775.
- _[81]V. K. Miloslav, P. S. Pogrebni, *Phys. Status Solidi B* **1972**, *51*, K99.
- _[82] R. K. Shukla, A. Srivastava, K. C. Dubey, *J. Cryst. Growth* **2006**, *294*, 427.

- _[83]J. H. Wang, L. Meng, Y. Qi, M. L. Li, G. M. Shi, M. L. Liu, *J. Cryst. Growth* **2009**, *311*, 2305.
- _[84]K. F. Berggren, B. E. Sernelius, *Physical Review B* **1981**, *24*, 1971.
- _[85]C. Soci, A. Zhang, B. Xiang, S. A. Dayeh, D. P. R. Aplin, J. Park, X. Y. Bao, Y. H. Lo, D. Wang, *Nano Lett.* **2007**, *7*, 1003.
- _[86]G. Eranna, B. C. Joshi, D. P. Runthala, R. P. Gupta, *Crit. Rev. Solid State Mater. Sci.* **2004**, *29*, 111.
- _[87]M. R. Hoffmann, S. T. Martin, W. Y. Choi, D. W. Bahnemann, *Chem. Rev.* **1995**, *95*, 69.
- _[88]K. Nomura, H. Ohta, K. Ueda, T. Kamiya, M. Hirano, H. Hosono, *Science* **2003**, *300*, 1269.
- _[89]B. Oregan, M. Gratzel, *Nature* **1991**, *353*, 737.
- _[90]H. Kawazoe, H. Yanagi, K. Ueda, H. Hosono, *MRS Bull.* **2000**, *25*, 28.
- _[91]H. Sato, T. Minami, S. Takata, T. Yamada, *Thin Solid Films* **1993**, *236*, 27.
- _[92]H. Raebiger, S. Lany, A. Zunger, *Physical Review B* **2007**, *76*.
- _[93]S. Narushima, H. Mizoguchi, K. Shimizu, K. Ueda, H. Ohta, M. Hirano, T. Kamiya, H. Hosono, *Adv. Mater.* **2003**, *15*, 1409.
- _[94]V. V. Mokrousov, *Izv. Vuz. Fiz.* **1970**, 113.
- _[95]W. Y. Lee, D. Mauri, C. Hwang, *Appl. Phys. Lett.* **1998**, *72*, 1584.
- _[96]H. Ohta, M. Hirano, K. Nakahara, H. Maruta, T. Tanabe, M. Kamiya, T. Kamiya, H. Hosono, *Applied Physics Letters* **2003**, *83*, 1029.
- _[97]J. Katayama, K. Ito, M. Matsuoka, J. Tamaki, *J. Appl. Electrochem.* **2004**, *34*, 687.

- _[98]H. Tanaka, T. Shimakawa, T. Miyata, H. Sato, T. Minami, *Appl. Surf. Sci.* **2005**, *244*, 568.
- _[99]M. Izaki, K. Mizuno, T. Shinagawa, M. Inaba, A. Tasaka, *Journal of the Electrochemical Society* **2006**, *153*, C668.
- _[100]T. Minami, T. Miyata, K. Ihara, Y. Minamino, S. Tsukada, *Thin Solid Films* **2006**, *494*, 47.
- _[101]M. Izaki, T. Shinagawa, K. T. Mizuno, Y. Ida, M. Inaba, A. Tasaka, *Journal of Physics D-Applied Physics* **2007**, *40*, 3326.
- _[102]S. S. Jeong, A. Mittiga, E. Salza, A. Masci, S. Passerini, *Electrochim. Acta* **2008**, *53*, 2226.
- _[103]A. Kudo, H. Yanagi, K. Ueda, H. Hosono, H. Kawazoe, Y. Yano, *Appl. Phys. Lett.* **1999**, *75*, 2851.
- _[104]K. Tonooka, H. Bando, Y. Aiura, *Thin Solid Films* **2003**, *445*, 327.
- _[105]J. Bullo, O. Gallais, M. Gauthier, J. Livage, *Appl. Phys. Lett.* **1980**, *36*, 986.
- _[106]J. Livage, *Chem. Mater.* **1991**, *3*, 578.
- _[107]J. Bullo, P. Cordier, O. Gallais, M. Gauthier, J. Livage, *J Non-Cryst Solids* **1984**, *68*, 123.
- _[108]J. C. Badot, S. Ribes, E. B. Yousfi, V. Vivier, J. P. Pereira-Ramos, N. Baffier, D. Lincot, *Electrochem. Solid-State Lett.* **2000**, *3*, 485.
- _[109]J. Musschoot, D. Deduytsche, H. Poelman, J. Haemers, R. L. Van Meirhaeghe, S. Van den Berghe, C. Detavernier, *J. Electrochem. Soc.* **2009**, *156*, P122.
- _[110]A. A. Bahgat, A. Al-Hajry, M. M. El-Desoky, *physica status solidi (a)* **2006**, *203*, 1999.

- _[111]P. Aldebert, H. W. Haesslin, N. Baffier, J. Livage, *J. Colloid Interface Sci.* **1984**, 98, 478.
- _[112]P. Aldebert, N. Baffier, N. Gharbi, J. Livage, *Mater. Res. Bull.* **1981**, 16, 669.
- _[113]P. Banerjee, W. J. Lee, K. R. Bae, S. B. Lee, G. W. Rubloff, *Journal of Applied Physics* **2010**, 108.
- _[114]N. F. Mott, E. A. Davis, *Philos Mag* **1968**, 17, 1269.
- _[115]J. C. Badot, N. Baffier, *J Mater Chem* **1992**, 2, 1167.
- _[116] W. Brutting, H. Riel, T. Beierlein, W. Riess, *J. Appl. Phys.* **2001**, 89, 1704.
- _[117]S. Hioki, T. Ohishi, K. Takahashi, T. Nakazawa, *Nippon Seram Kyo Gak* **1989**, 97, 628.
- _[118]A. L. Pergament, E. L. Kazakova, G. B. Stefanovich, *J. Phys. D: Appl. Phys.* **2002**, 35, 2187.
- _[119]P. Kounavis, A. Vomvas, E. Mytilineou, M. Roilos, L. Murawski, *J. Phys. C: Solid State* **1988**, 21, 967.
- _[120]J. C. Badot, A. Mantoux, N. Baffier, O. Dubrunfaut, D. Lincot, *J Mater Chem* **2004**, 14, 3411.
- _[121]Y. J. Liou, R. A. Hudson, S. K. Wonnell, L. M. Slifkin, *Phys Rev B* **1990**, 41, 10481.
- _[122]A. S. Arico, P. Bruce, B. Scrosati, J. M. Tarascon, W. Van Schalkwijk, *Nature Materials* **2005**, 4, 366.
- _[123]J. W. Long, B. Dunn, D. R. Rolison, H. S. White, *Chemical Reviews* **2004**, 104, 4463.

_[124]K. A. Arpin, A. Mihi, H. T. Johnson, A. J. Baca, J. A. Rogers, J. A. Lewis, P. V. Braun, *Advanced Materials* **2010**, *22*, 1084.

_[125]H. Masuda, F. Hasegawa, S. Ono, *Journal of the Electrochemical Society* **1997**, *144*, L127.

_[126]A. P. Li, F. Muller, A. Birner, K. Nielsch, U. Gosele, *Advanced Materials* **1999**, *11*, 483.

_[127]P. Banerjee, X. Chen, K. Gregorczyk, L. Henn-Lecordier, G. W. Rubloff, *Advanced Functional Materials* **Submitted**.